CHALMERS
UNIVERSITY OF TECHNOLOGY

Mismatch Analysis and Cooperative Calibration of Array Beam Patterns for ISAC Systems

Mismatch Analysis and Cooperative Calibration of Array Beam Patterns for ISAC Systems

Hui Chen, *Member, IEEE*, Mengting Li, *Member, IEEE*, Alireza Pourafzal, *Member, IEEE*, Huiping Huang, *Member, IEEE*, Yu Ge, *Member, IEEE*, Sigurd Sandor Petersen, Ming Shen, *Senior Member, IEEE*, George C. Alexandropoulos, *Senior Member, IEEE*, and Henk Wymeersch, *Fellow, IEEE*

***Abstract*—Integrated sensing and communication (ISAC) is a key technology for enabling a wide range of applications in future wireless systems. However, the sensing performance is often degraded by model mismatches caused by geometric errors (e.g., position and orientation) and hardware impairments (e.g., mutual coupling and amplifier non-linearity). This paper focuses on the angle estimation performance with antenna arrays and tackles the critical challenge of array beam pattern calibration for ISAC systems. To assess calibration quality from a sensing perspective, a novel performance metric that accounts for angle estimation error, rather than beam pattern similarity, is proposed and incorporated into a differentiable loss function. Additionally, a cooperative calibration framework is introduced, allowing multiple user equipments to iteratively optimize the beam pattern based on the proposed loss functions and local data, and collaboratively update global calibration parameters. The proposed models and algorithms are validated using real-world beam pattern measurements collected in an anechoic chamber. Experimental results show that the angle estimation error can be reduced from 1.01° to 0.11° in 2D calibration scenarios, and from 5.19° to 0.86° in 3D calibration scenarios.**

***Index Terms*—ISAC, array beam pattern, cooperative calibration, mismatch analysis, stochastic gradient descent.**

Received 27 November 2025; revised 18 March 2026; accepted 16 April 2026. Date of publication 4 May 2026; date of current version 6 May 2026. This work was supported in part by the Research Grant from VILLUM FONDEN under Grant VIL59841, in part by Swedish Research Council Vetenskapsrådet (VR) under Grant 2022-03007, in part by the Smart Networks and Services Joint Undertaking (SNS JU) Project 6G-DISAC through the EU's Horizon Europe Research and Innovation Program under Grant 101139130, in part by the Vinnova B5GPOS Project under Grant 2022-01640, in part by the Chalmers Area-of-Advance Transport under Project 95418010, and in part by European Union's Horizon Europe Research and Innovation Program through the Marie Skłodowska-Curie under Grant 101207620 (MIDAS-6G) and Grant 101201808 (SMALL-6G). The associate editor coordinating the review of this article and approving it for publication was F. Fang. *(Corresponding author: Mengting Li.)*

Hui Chen is with the Department of Electrical Engineering, Chalmers University of Technology, 412 58 Gothenburg, Sweden, and also with the Department of Electronic and Electrical Engineering, University College London, WC1E 7JE London, U.K. (e-mail: hui.chen@chalmers.se; hui.chen@ucl.ac.uk).

Mengting Li is with the Department of Electrical Engineering, Chalmers University of Technology, 412 58 Gothenburg, Sweden, and also with Aalborg University, 9220 Aalborg, Denmark (e-mail: limeng@chalmers.se).

Alireza Pourafzal, Huiping Huang, Yu Ge, and Henk Wymeersch are with the Department of Electrical Engineering, Chalmers University of Technology, 412 58 Gothenburg, Sweden (e-mail: alireza.pourafzal@chalmers.se; huiping@chalmers.se; yuge@chalmers.se; henkw@chalmers.se).

Sigurd Sandor Petersen and Ming Shen are with Aalborg University, 9220 Aalborg, Denmark (e-mail: sp19@student.aau.dk; mish@es.aau.dk).

George C. Alexandropoulos is with the Department of Informatics and Telecommunications, National and Kapodistrian University of Athens, 16122 Athens, Greece (e-mail: alexandg@di.uoa.gr).

Digital Object Identifier 10.1109/TWC.2026.3687249

I. Introduction

INTEGRATED sensing and communication (ISAC) is becoming a central pillar of next-generation wireless systems to provide location information and environment awareness [1]. With large array apertures and wide bandwidths, the communication signals enable not only higher data rates but also finer angular and delay resolutions [2]. In addition to traditional time-of-arrival (TOA) and time-difference-of-arrival (TDOA) methods, angle-based measurements, such as angles-of-arrival (AOA) and angles-of-departure (AOD), are now integrated into standardized systems like 3GPP NR [3]. Such angle measurements provide substantial improvements in localization coverage and accuracy and enable complex tasks, including multipath-aided single base station (BS) localization [4], device orientation estimation [5], and simultaneous localization and mapping (SLAM) [6]. These developments point toward a future in which 6G networks will support a diverse array of ISAC-driven services, from extended reality to autonomous navigation [7].

Despite the significant potential of ISAC, most current studies assume ideal system models and overlook the effects of calibration errors, such as geometric error [8] and hardware impairments [9]. While these assumptions facilitate performance analysis and the development of low-complexity algorithms (including super-resolution techniques for channel parameter estimation [10], [11]), model mismatches lead to system performance degradation. Inaccurate beamforming caused by such mismatches reduces array gain, increases interference, and degrades link reliability [12]. In sensing applications, the consequences are even more pronounced, as angular errors amplify with distance and can severely degrade system performance.[1] These inaccuracies affect the performance of channel parameter extraction and subsequent high-level tasks such as localization and mapping [13]. This indicates that array calibration is needed to fully harness the potential of communication systems for sensing.

[1]The signal-to-noise ratio (SNR) degradation caused by an angle-estimation error $\Delta\theta$ in an $N \times 1$ uniform linear array (ULA) with half-wavelength inter-element spacing is given by $\mathrm{SNR}_{\mathrm{loss}} = \left|\frac{1}{N}\sum_{n=0}^{N-1} e^{j\pi n(\sin\theta - \sin(\theta+\Delta\theta))}\right|^2$, while the corresponding location error due to this angular error at distance r is $\Delta x = r\,|\tan(\theta+\Delta\theta) - \tan(\theta)|$. For a user at $\theta = 0°$ and $r = 100$ m with $\Delta\theta = 1°$ and $N = 8$, the SNR degradation and distance error are 0.069 dB and 1.75 m, respectively.

TABLE I
SUMMARY OF BEAM PATTERN CALIBRATION METHODS

Ref.	Purpose (Calibration Focus)	Hardware Type (Array Size)	Scenario	Key Methodology
[14]	5G array error calibration	Digital array (4-element)	In situ	Expectation–maximization with interference cancellation
[15]	SLAC: joint position + calibration	Digital array (up to 4)	Self-calibration	Bayesian filtering, orientation, bias estimation
[16]	Beam pattern characterization	Phased array (4×5)	Offline	REV method (element-wise phase sweep)
[17]	Fast REV-based calibration	Phased array (4×5)	Offline	Enhanced REV (multi-element switching)
[18]	Amplitude-only calibration	Phased array (4×5)	Offline	Fourier-based recovery from amplitude sweeps
[19]	Amplitude-only fast calibration	Phased array (8-element)	Offline	3-phase shift measurement (0°, 90°, 180°)
[20]	Simultaneous element calibration	Phased array (8-element)	Offline	Linear system solver using all-on measurements
[21]	Reduced measurement load	Phased array (4×8)	Offline	Sparse measurement, linear recovery
[22]	OTA beam-mode calibration	Phased array (4×4)	Offline	Calibration in beam-steering mode only
[23]	Mutual coupling-aware modeling	RIS (up to 4×8)	Self-calibration	Electromagnetic end-to-end circuit model
[24]	OTA phase calibration	RIS (8×8)	In situ	Alternating block descent, CRB benchmark
[25]	MC-aware localization	RIS (20×20)	Self-calibration	Alternating optimization for joint localization and calibration
[26]	Excitation vector learning	Phased array (up to 4×8)	Offline	Transfer-learning-based surrogate model (power-only)
[27]	Antenna displacement calibration	Phased array (8×8)	Self-calibration	Model-driven learning-based ISAC under hardware impairment
Ours	Sensing-based calibration	Phased array (up to 16×16)	In situ	Response and angle error loss based optimization

A. Related Works

Array calibration scenarios can be broadly categorized into offline calibration (e.g., in a chamber or controlled environment with a dedicated calibration process), in situ calibration with known calibration agent state, and self-calibration that can calibrate the array without additional devices [14], as shown in Table I. Generally, offline calibration achieves the highest accuracy but requires specialized setups, whereas in situ and self-calibration methods are more practical in real deployments, with the former relying on a dedicated calibration agent. In terms of calibration methods, they can be classified into element pattern calibration, amplitude-only calibration, complex-valued/structure-aware calibration, and artificial intelligence (AI)-based calibration. In the following, we review the state-of-the-art in each category and discuss their applicability and limitations for ISAC systems.

1) Element Pattern Calibration: Element calibration focuses on estimating element-wise antenna response. In [14], the calibration problem is framed as the estimation of an array error function (gain and phase error for each antenna), with experimental validation on a 4×1 antenna array. With the cooperation of multiple mobile agents, [15] presents a simultaneous localization and calibration (SLAC) approach that uses Bayesian filtering to estimate positions and calibration parameters in mobile networks jointly. While effective, such methods are generally limited to small-scale or linear arrays and do not scale efficiently to large or hybrid analog-digital arrays.

2) Amplitude-Only Calibration: Amplitude-only calibration methods, such as the widely-used rotating element electric field vector (REV) method and its variations [16], [17], [18], enable antenna array calibration by introducing additional phase shifters to perform element-wise phase sweeps and reconstruct the array response using only amplitude measurements. Enhanced REV methods, such as multi-element switching [17] and Fourier-based recovery [18], further reduce calibration time and complexity. The fast amplitude-only calibration in [19] employs three-phase shift measurements (0°, 90°, 180°). Amplitude-only methods are particularly valuable when accurate phase measurements are unavailable or impractical; however, they fail to fully restore the complex beam pattern, limiting their effectiveness for angle estimation and high-precision sensing. Additionally, these methods often require hardware modifications (such as extra phase shifters), which may not be feasible for all array architectures, especially in the context of hybrid or distributed ISAC deployments.

3) Complex-Valued and Structure-Aware Calibration: The third category of calibration techniques leverages linear algebraic structures and advanced modeling to reduce the number of required calibration measurements or to account for mutual coupling and hardware impairments. For example, [20], [21], [22] exploit linear system formulations and sparse recovery methods for calibration, reducing measurement overhead. In the context of reconfigurable intelligent surfaces (RISs), impedance-based modeling has been proposed to describe mutual coupling [23], while alternating optimization-based approaches have demonstrated high performance in over-the-air (OTA) tests with complex propagation environments [24] and joint localization and calibration scenarios [25]. These methods can provide accurate calibration in the presence of hardware non-idealities, but they often require access to detailed hardware parameters, precise control over system operation, or additional measurement campaigns. Furthermore, the assumptions made regarding array geometry, mutual coupling, or propagation environment may not generalize well to large-scale, distributed, or hybrid analog-digital systems.

4) AI-Based Calibration: Recent advances in data-driven calibration approaches aim to address practical challenges in dynamic and distributed environments. In [26], a surrogate-model-based method is introduced for phased array calibration using only power measurements, leveraging transfer learning to adapt excitation vector models across devices. Model-driven deep learning frameworks have also shown promise for correcting antenna displacement errors [27]. These AI-based methods are attractive for large-scale and practical deployments, as they can learn from real-world data and adapt to changing conditions. However, they typically focus on beam pattern reconstruction accuracy and do not directly address the impact of calibration on sensing accuracy. Moreover, these approaches often require extensive training data and may not be robust to all types of hardware impairments or environmental dynamics.

While the above calibration methods offer valuable solutions for specific scenarios, most existing works evaluate calibration quality based on beam pattern reconstruction accuracy, without explicitly quantifying the impact of beam mismatch

on sensing or localization performance. Additionally, much of the literature assumes fully digital architectures or fixed array types, overlooking the analog and hybrid beamforming structures and distributed calibration needs common in practical millimeter wave (mmWave) ISAC systems. In emerging reconfigurable platforms incorporating movable antennas and RIS [28], calibration becomes even more challenging due to array reconfiguration, element-wise phase errors, coupling effects, and limited feedback. Such systems introduce additional calibration overhead and require scalable, possibly distributed, calibration mechanisms to remain robust against hardware non-idealities. These limitations reduce the practical relevance of current calibration methods for real-world sensing and localization tasks.

It is worth noting that mismatches caused by array beam patterns can also be mitigated through robust beamforming techniques, which introduce tolerance to uncertainties in, e.g., channel state information [29] and user location [30]. Compared with the proposed calibration approach, robust beamforming focuses on maintaining acceptable performance under model uncertainties rather than correcting the underlying beam-pattern distortions. As a result, robust beamforming typically adopts conservative designs to guarantee worst-case performance, which may lead to a performance gap compared to a well-calibrated system where accurate beam patterns enable more efficient beamforming.

B. Contributions

In this work, we address in situ beam pattern calibration using downlink pilot signals from a sensing-oriented perspective: we quantify how beam mismatch degrades localization accuracy, and we develop both a practical beam pattern model and a scalable cooperative calibration algorithm suitable for distributed implementation under hybrid beamforming constraints.

The main contributions of this paper are as follows:

- We formulate a cooperative beam calibration problem in a distributed integrated sensing and communication (ISAC) scenario. Array calibration of the BS is performed at each user equipment (UE) via communication pilot signals, and multiple UEs collaborate to jointly calibrate the beam pattern of the BS antenna array, as illustrated in Fig. 1.
- We develop a novel, sensing-oriented performance metric, obtained by calculating the pseudo-true parameter that minimizes the Kullback-Leibler divergence between the actual model and the mismatched model after calibration. Unlike traditional beam pattern similarity metrics, the proposed metric better reflects calibration quality in terms of sensing performance.
- We propose an iterative optimization algorithm adopting a differentiable objective function, approximated from the sensing-based performance metric. The algorithm can further refine communication-based calibration for better sensing performance and support cooperation between multiple calibration agents.
- We validate the proposed beam pattern models and calibration algorithms based on real-world beam pattern measurements in an anechoic chamber. Both communication- and sensing-oriented performance metrics are assessed across various scenarios and hyperparameter settings.

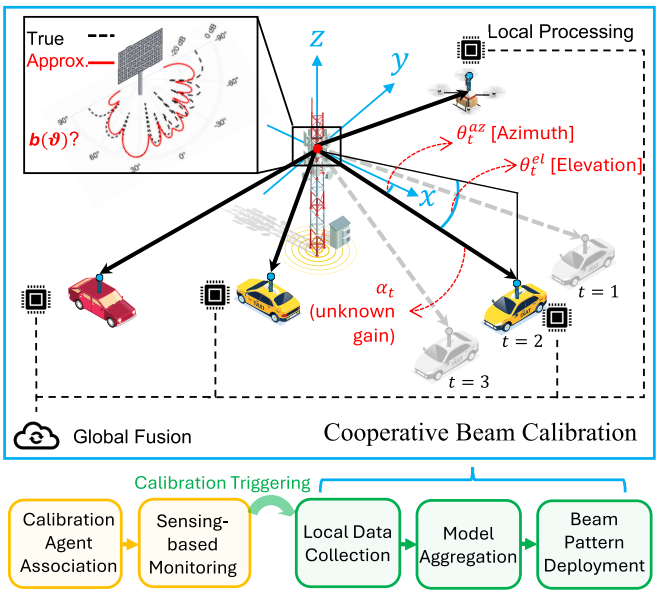

Fig. 1. Illustration of the considered cooperative beam calibration scenario and the calibration procedure. Local calibrated array beam patterns are obtained from cooperative UEs and then fused globally.

Notations and Symbols: Italic letters denote scalars (e.g., a), bold lower-case letters denote vectors (e.g., $\mathbf{a}$), and bold upper-case letters denote matrices (e.g., $\mathbf{A}$). $(\cdot)^\top$, $(\cdot)^\mathsf{H}$, $(\cdot)^*$, $(\cdot)^{-1}$, $\mathrm{tr}(\cdot)$, $\|\cdot\|$, and $\|\cdot\|_\mathrm{F}$ represent the transpose, Hermitian transpose, complex conjugate, inverse, trace, ℓ-2 norm, and Frobenius norm operations, respectively; $\mathbf{A}\odot\mathbf{B}$, $\mathbf{A}\oslash\mathbf{B}$, $\mathbf{A}\otimes\mathbf{B}$, $\mathbf{a}\circ\mathbf{b}$ are the Hadamard product, Hadamard division, Kronecker product, and outer product, respectively; $[\cdot, \cdot, \cdots, \cdot]^\top$ denotes a column vector; $[\cdot]_{i,j}$ is the element in the i-th row, j-th column of a matrix, and $[\cdot]_{a:b,c:d}$ is the submatrix constructed from the a-th to the b-th row, and the c-th to d-th column of a matrix; $\mathrm{Re}\{a\}$ and $\mathrm{Im}\{a\}$ extract the real and imaginary parts of a complex variable, $\angle(a)$ denotes the phase of a complex scalar a; $\mathbf{1}_N$ denotes an $N \times 1$ all-ones vector, and $\mathbf{I}_N$ denotes a size-N identity matrix.

II. System Model

In this section, we begin with a general system model that includes geometrical information about the transmitter and receiver, as well as the beam pattern. Then, several beam representations will be described, followed by the corresponding calibration models.

A. Generic System Model

We consider a far-field orthogonal frequency division multiplexing (OFDM)-based downlink system with one BS and multiple UEs. For simplicity, we describe the system model for a specific BS-UE link, and thus the UE index is dropped throughout this section. The BS located at $\mathbf{p}_\mathrm{B} \in \mathbb{R}^3$ is equipped with an analog uniform planar array consisting of $N = N_r \times N_c$ antennas (N_r rows and N_c columns), and a single-antenna UE moves alone a predefined trajectory (e.g.,

from $\mathbf{p}_{\mathrm{U},1} \in \mathbb{R}^3$ to $\mathbf{p}_{\mathrm{U},T}$ with a total of T snapshots) and receives pilot signals from the BS.[2] At snapshot t, G OFDM symbols are transmitted from BS to UE, each with K subcarriers and a unique beamforming vector (forming a G-codeword beam sweeping), and the received signals $\mathbf{Y}_t \in \mathbb{C}^{G\times K}$ can be expressed as the combination of signals propagating $L+1$ paths given by

$$\mathbf{Y}_t = \sum_{\ell=0}^{L} \alpha_{\ell,t}\mathbf{b}(\boldsymbol{\vartheta}_{\ell,t})(\mathbf{d}(\tau_{\ell,t}) \odot \mathbf{x}_t)^\top + \mathbf{N}_t, \tag{1}$$

where ℓ is the index of path with $\ell = 0$ denoting the line-of-sight (LOS) path, $\alpha_{0,t} = \sqrt{P}\frac{\lambda}{4\pi r_{0,t}}e^{j\beta_{0,t}}$ is the LOS complex channel gain with P as the transmit power, $\beta_{0,t}$ as the phase, and $r_0 = \|\mathbf{p}_{\mathrm{B}} - \mathbf{p}_{\mathrm{U}}\|$ as the distance between the t-th measurement location and the BS array. The channel gain of the non-line-of-sight (NLOS) path ($\ell > 0$) can be expressed as $\alpha_{\ell,t} = \sqrt{P}\frac{c_\ell}{\sqrt{4\pi}}\frac{\lambda}{4\pi r_{\ell,t,1}r_{\ell,t,2}}e^{j\beta_{\ell,t}}$, with c_ℓ as the radar cross-section coefficient, $r_{\ell,t,2} = \|\mathbf{p}_{\mathrm{B}} - \mathbf{p}_{\mathrm{S},\ell,t}\|$ and $r_{\ell,t,1} = \|\mathbf{p}_{\mathrm{U}} - \mathbf{p}_{\mathrm{S},\ell,t}\|$ denoting the distances from the BS and UE to the scattering point (located at $\mathbf{p}_{\mathrm{S},\ell,t}$), respectively. Angle pair $\boldsymbol{\vartheta}_{\ell,t} = [\theta^{\mathrm{az}}_{\ell,t}, \theta^{\mathrm{el}}_{\ell,t}]^\top$ is the AOD in both azimuth and elevation, $\tau_{\ell,t}$ is the signal delay. The pilot signal vector is denoted by $\mathbf{x}_t \in \mathbb{C}^K$ with constant modulus as $|x_{t,g}| = 1$, and $\mathbf{N}_t \in \mathbb{C}^{G\times K}$ is the additive white Gaussian noise matrix with each element $n_{t,g} \in \mathcal{CN}(0, \sigma_n^2)$. The beam response vector (for G codewords) at a specific angle pair $\boldsymbol{\vartheta}$ is denoted as $\mathbf{b}(\boldsymbol{\vartheta}) = [b_1(\boldsymbol{\vartheta}), \ldots, b_G(\boldsymbol{\vartheta})]^\top \in \mathbb{C}^G$, which will be detailed in the following subsection, and $\mathbf{d}(\tau) \in \mathbb{C}^K$ reflects the phase offset across different subcarriers with each element $d_k(\tau) = e^{j2\pi k\Delta_f \tau}$, where τ is the delay and Δ_f is the subcarrier spacing. A detailed geometric relationship between the BS/UE position, orientation, and channel parameters can be found in [2].

By de-rotating the phase caused by the LOS delay $\hat{\tau}_{0,t}$, removing the pilot signals as $\mathbf{Y}_t \oslash (\mathbf{1}_G \mathbf{x}_t^\top)$, and coherently combining the K subcarriers, the generic system model can be simplified from (1) as

$$\mathbf{y}_t = \underbrace{\tilde{\gamma}_t \mathbf{b}(\boldsymbol{\vartheta}_t)}_{\text{LOS path}} + \underbrace{\sum_{\ell=1}^{L} \alpha_{\ell,t}\mathbf{b}(\boldsymbol{\vartheta}_{\ell,t})\mathbf{d}^{\mathsf{H}}(\hat{\tau}_{0,t})\mathbf{d}(\tau_{\ell,t})}_{\text{NLOS paths}} + \mathbf{n}_t. \tag{2}$$

Here, $\boldsymbol{\vartheta}_t$ denotes $\boldsymbol{\vartheta}_{0,t}$ by ignoring the subscript, $\tilde{\gamma}_t = \tilde{\gamma}_{0,t} = \alpha_{\ell,t}\mathbf{d}^{\mathsf{H}}(\hat{\tau}_{0,t})\mathbf{d}(\tau_{0,t})$ with $\hat{\tau}_{0,t}$ as the estimated LOS delay, and the noise level is scaled as $n_{t,g} \in \mathcal{CN}(0, K\sigma_n^2)$. We further assume that the bandwidth is sufficiently wide to resolve the delays of the LOS path and NLOS paths [11], and the NLOS path term in (2) be approximated to zero.[3] By concatenating beam pattern vectors for all the codewords into a matrix $\mathbf{B}(\boldsymbol{\Theta}) \in \mathbb{C}^{G\times T}$ with $\boldsymbol{\Theta} = [\boldsymbol{\vartheta}_1, \ldots, \boldsymbol{\vartheta}_T]$, we obtain

$$\mathbf{Y} = \mathbf{B}(\boldsymbol{\Theta})\tilde{\boldsymbol{\Gamma}} + \mathbf{N}. \tag{3}$$

Here, $\mathbf{Y} \in \mathbb{C}^{G\times T}$ contains all the measurements from T position/angles for a specific UE, and $\tilde{\boldsymbol{\Gamma}} = \mathrm{diag}([\tilde{\gamma}_1, \ldots, \tilde{\gamma}_T])$ contains the LOS complex channel gain for each measurement.

B. Beam Representation Model

The goal of beam representation is to find a simplified model to represent $\mathbf{B}(\boldsymbol{\Theta})$ and characterize the ground truth beam patterns (e.g., measured from a chamber). We adopt two beam representation models, namely, an ideal model (steering-based codebook with fixed beamforming directions) and a practical model (learned codebook). The former model is widely used in existing works [1], [5], [8], [9], [10] and will be used as a benchmark for the latter practical model.

1) Ideal Beam Model: Without loss of generality, we define an ideal array response at angle $\boldsymbol{\vartheta}$ as

$$\tilde{\mathbf{b}}(\boldsymbol{\vartheta}) = g(\boldsymbol{\vartheta})\bar{\mathbf{W}}^{\mathsf{H}}(\bar{\boldsymbol{\Phi}})\mathbf{a}(\boldsymbol{\vartheta}), \tag{4}$$

where $g(\boldsymbol{\vartheta})$ is the element pattern.[4] A simple patch antenna model can be implemented as [31]

$$g(\boldsymbol{\vartheta}, \beta) = \cos^{\beta}(\theta_{\mathrm{eff}}) = (\cos\theta^{\mathrm{az}}\cos\theta^{\mathrm{el}})^{\beta} \tag{5}$$

with $\theta_{\mathrm{eff}} = \cos^{-1}(\cos\theta^{\mathrm{az}}\cos\theta^{\mathrm{el}})$ being the effective angle between the target direction and the array boresight, and $\beta > 0$ is the directivity parameter. However, the following calibration tasks are not limited to the beam pattern model defined in (5). The steering vector $\mathbf{a}(\boldsymbol{\vartheta})$ captures the phase differences due to array configuration across different antennas (assuming half-wavelength spacing) as[5]

$$\mathbf{a}(\boldsymbol{\vartheta}) = \mathbf{a}_c(\theta^{\mathrm{az}}, \theta^{\mathrm{el}}) \otimes \mathbf{a}_r(\theta^{\mathrm{el}}), \tag{6}$$

with

$$\mathbf{a}_c(\theta^{\mathrm{az}}, \theta^{\mathrm{el}}) = [1, \ \cdots, \ e^{j\pi(N_c-1)\sin\theta^{\mathrm{az}}\cos\theta^{\mathrm{el}}}]^\top, \tag{7}$$

$$\mathbf{a}_r(\theta^{\mathrm{el}}) = [1, \ \cdots, \ e^{j\pi(N_r-1)\sin\theta^{\mathrm{el}}}]^\top. \tag{8}$$

In the ideal model, each codeword in the precoding matrix (or codebook) $\bar{\mathbf{W}}(\bar{\boldsymbol{\Phi}}) = [\mathbf{w}(\bar{\boldsymbol{\varphi}}_1), \ldots, \mathbf{w}(\bar{\boldsymbol{\varphi}}_G)] \in \mathbb{C}^{N\times G}$ is defined the same as the steering vector (e.g., $\mathbf{w}(\boldsymbol{\varphi}) = \mathbf{a}(\boldsymbol{\varphi})$) with the constraints $|w_{g,n}| = 1$, and $\boldsymbol{\varphi} = [\phi^{\mathrm{az}}, \phi^{\mathrm{el}}]^\top$ is the beamforming direction. Thus, each codeword maximizes the SNR at a certain direction $\bar{\boldsymbol{\varphi}}_g$, and $\bar{\mathbf{W}}$ can be represented by a set of beamforming angles $\bar{\boldsymbol{\Phi}} = [\bar{\boldsymbol{\varphi}}_1, \ldots, \bar{\boldsymbol{\varphi}}_G] \in \mathbb{C}^{2\times G}$ (predefined by the array manufacturer).

2) Practical Beam Model: As investigated in our initial work in [32], an ideal codebook can lead to severe mismatch and performance degradation. Alternatively, a practical codebook $\mathbf{W}$ (with each codeword satisfying $\|\mathbf{w}_g\| = 1$) capturing hardware limitations and realization issues can be defined as[6]

$$\mathbf{W} = \bar{\mathbf{W}}(\bar{\boldsymbol{\Phi}}) + \Delta_{\mathbf{W}}. \tag{9}$$

[2]This work uses downlink signals to highlight cooperative calibration in a distributed system, and the feedback between UEs and BS is needed to provide calibrated parameters. The calibration problem can also be performed using uplink signals with proper interference management.

[3]The subsequent likelihood derivation and loss construction assume an LOS-dominant single-path channel model. However, when strong unresolved multipath components are present, this assumption no longer holds, resulting in model mismatch.

[4]At the UE side, element pattern should also be considered. However, we will show in Sec. II-C that the element patterns of both UE and BS do not affect sensing performance and hence are treated as nuisance parameters.

[5]The steering vector corresponds to a far-field plane-wave model, where the array response depends only on the angular direction. In near-field scenarios, spherical wavefront propagation introduces joint range–angle dependence, requiring a location-dependent steering model. Such extensions are left for future investigation.

[6]Note that the definition of $\mathbf{W}$ could be either $\bar{\mathbf{W}}(\bar{\boldsymbol{\Phi}}) + \Delta_{\mathbf{W}}$ or $\bar{\mathbf{W}}(\bar{\boldsymbol{\Phi}}) \odot \Delta_{\mathbf{W}}$. Since we estimate $\mathbf{W}$ as a whole without access to $\Delta_{\mathbf{W}}$, the choice of these two forms does not affect calibration.

Hence, the beam pattern model of a specific direction can further be defined as

$$\mathbf{b}(\boldsymbol{\vartheta}) = g(\boldsymbol{\vartheta})\mathbf{W}^{\mathsf{H}}\mathbf{a}(\boldsymbol{\vartheta}). \tag{10}$$

While more complex impairment models exist (e.g., array gain error considered in [9]), the formulation in (10) is an approximation that yields accurate calibration performance with reduced complexity, which will be the main focus of this work.

C. Sensing Model

Given a beam representation model, the sensing task can be defined as extracting the angle $\boldsymbol{\vartheta}$ from the observed signal $\mathbf{y}$. Since the beam pattern error has a limited effect on delay estimation [9], we focus on angle estimation based on maximum likelihood estimator (MLE). We show that, based on the model in (3), sensing relies only on the codebook $\mathbf{W}$, and the channel gain matrix $\boldsymbol{\Gamma}$ is a nuisance parameter for sensing-based calibration.

The angle estimation for the LOS scenario can be formulated as [33]

$$[\boldsymbol{\vartheta}, \alpha] = \arg\min_{\boldsymbol{\vartheta},\alpha} \|\mathbf{y} - \alpha\mathbf{b}(\boldsymbol{\vartheta})\|, \tag{11}$$

where $\mathbf{y}$ is an observation vector for a specific location. To simplify the estimation, the nuisance parameter α can be represented as $\alpha = \frac{\mathbf{b}^{\mathsf{H}}(\boldsymbol{\vartheta})\mathbf{y}}{\mathbf{b}^{\mathsf{H}}(\boldsymbol{\vartheta})\mathbf{b}(\boldsymbol{\vartheta})}$ based on (11) with a given $\boldsymbol{\vartheta}$, and the estimation problem can be written as [33]

$$\begin{aligned}\boldsymbol{\vartheta} &= \arg\min_{\boldsymbol{\vartheta}} \|\mathbf{y} - \frac{\mathbf{b}^{\mathsf{H}}(\boldsymbol{\vartheta})\mathbf{y}}{\mathbf{b}^{\mathsf{H}}(\boldsymbol{\vartheta})\mathbf{b}(\boldsymbol{\vartheta})}\mathbf{b}(\boldsymbol{\vartheta})\|^2 \\ &= \arg\min_{\boldsymbol{\vartheta}} \mathbf{y}^{\mathsf{H}}\mathbf{y} - \frac{\mathbf{b}^{\mathsf{H}}(\boldsymbol{\vartheta})\mathbf{y}}{\mathbf{b}^{\mathsf{H}}(\boldsymbol{\vartheta})\mathbf{b}(\boldsymbol{\vartheta})}\mathbf{y}^{\mathsf{H}}\mathbf{b}(\boldsymbol{\vartheta}) \\ &= \arg\max_{\boldsymbol{\vartheta}} \frac{|\mathbf{b}^{\mathsf{H}}(\boldsymbol{\vartheta})\mathbf{y}|}{\|\mathbf{b}(\boldsymbol{\vartheta})\|} = \arg\max_{\boldsymbol{\vartheta}} \frac{|\mathbf{a}^{\mathsf{H}}(\boldsymbol{\vartheta})\mathbf{W}\mathbf{y}|}{\|\mathbf{W}^{\mathsf{H}}\mathbf{a}(\boldsymbol{\vartheta})\|}. \end{aligned} \tag{12}$$

Here, the nuisance parameter α is eliminated, and the optimization is over $\boldsymbol{\vartheta}$ only. From (12) we can see that angle estimation is not related to the element pattern $g(\boldsymbol{\vartheta})$. However, to reconstruct the beam pattern for communication purposes, estimation of the element pattern is needed.

D. Calibration Models

The goal of this calibration work is to find a beam representation $\mathbf{b}(\boldsymbol{\vartheta})$ defined in (10), based on the received pilot signals $\mathbf{Y}$ in (3), such that the sensing performance in (11) can be improved. Next, we first describe the compact calibration model, followed by several calibration models. To assist calibration, we incorporate the element pattern (originally from $\mathbf{b}(\boldsymbol{\vartheta}_t)$ as shown in (10)) into the gain matrix $\tilde{\boldsymbol{\Gamma}}$ to form $\boldsymbol{\Gamma} = \text{diag}(\boldsymbol{\gamma})$ with each diagonal element as $\gamma_t = \tilde{\gamma}_t g(\boldsymbol{\vartheta}_t)$. Consequently, the generic system model can be reformulated from (3) as

$$\mathbf{Y} = \mathbf{W}^{\mathsf{H}}\mathbf{A}(\boldsymbol{\Theta})\boldsymbol{\Gamma} + \mathbf{N}, \tag{13}$$

with $\mathbf{A}(\boldsymbol{\Theta}) = [\mathbf{a}(\boldsymbol{\vartheta}_1), \ldots, \mathbf{a}(\boldsymbol{\vartheta}_T)] \in \mathbb{C}^{N\times T}$ as the steering matrix. Once the codebook $\hat{\mathbf{W}}$ and the gain matrix $\hat{\boldsymbol{\Gamma}}$ are obtained, the calibrated beam response can be expressed as

$$\hat{\mathbf{b}}(\boldsymbol{\vartheta}) = \hat{g}(\boldsymbol{\vartheta})\hat{\mathbf{W}}^{\mathsf{H}}\mathbf{a}(\boldsymbol{\vartheta}). \tag{14}$$

Since the gain estimate $\boldsymbol{\Gamma}$ corresponds to certain angles, we interpolate the element pattern $\hat{g}(\boldsymbol{\vartheta}_t) = r_t|\gamma_t|$ to obtain $\hat{g}(\boldsymbol{\vartheta})$, where r_t is the compensation of path loss. Note that the beam response $\mathbf{b}(\boldsymbol{\vartheta})$ reflects the complex response gain for different angles, and normalization will be performed when evaluating the calibration accuracy.

In this work, we assume UEs are dedicated calibration agents with known location[7] in each of the T measurements (e.g., from GPS), and hence the calibration task is to estimate the unknown parameters (e.g., codebook $\mathbf{W}$ and beam gain matrix $\boldsymbol{\Gamma}$, depending on the scenarios) and reconstruct the beam pattern $\mathbf{b}(\boldsymbol{\vartheta})$ for better communication and sensing performance. Next, we detail different calibration scenarios, where model M1 works as the benchmark for models M2-M4, and the main focus is on M4 throughout this work.

1) Benchmark Beam Pattern Model (M1): This model adopts an ideal codebook $\bar{\mathbf{W}}(\bar{\boldsymbol{\Phi}})$ with known beamforming directions $\bar{\boldsymbol{\Phi}}$. We assume the sample angle $\boldsymbol{\vartheta}_t$ and distance r_t are known for each measurement point, the calibration objective is to estimate the channel gain matrix $\boldsymbol{\Gamma}$ and then extract the element pattern as $g(\boldsymbol{\vartheta}_t) = r_t|\gamma_t|$. The corresponding signal model can be expressed as

$$\mathbf{Y}^{\text{M1}} = \bar{\mathbf{W}}^{\mathsf{H}}(\bar{\boldsymbol{\Phi}})\mathbf{A}(\bar{\boldsymbol{\Theta}})\boldsymbol{\Gamma} + \mathbf{N}. \tag{15}$$

From a sensing perspective, no calibration is needed for M1, and the $\boldsymbol{\Gamma}$ is estimated for beam reconstruction purposes.

2) Beamforming Angle Calibration (M2): Considering the inaccuracy of the beamforming angle provided by the array manufacturer, M2 focuses on the calibration of the matrices $\boldsymbol{\Phi}$ and $\boldsymbol{\Gamma}$ at the same time. The signal model in this case can be expressed as follows:

$$\mathbf{Y}^{\text{M2}} = \bar{\mathbf{W}}^{\mathsf{H}}(\boldsymbol{\Phi})\mathbf{A}(\bar{\boldsymbol{\Theta}})\boldsymbol{\Gamma} + \mathbf{N}. \tag{16}$$

Calibration M2 is expected to provide better performance than M1 with more accurate beamforming angles.

3) Codebook Calibration (M3): Codebook calibration can only be performed offline to remove the effect of channel gain (e.g., inside the chamber or a well-controlled environment). Then, the calibration task becomes estimating the codebook $\mathbf{W}$ and the directionality coefficient β defined in (5), assuming UE locations are known, and the signal model can be expressed as [22] and [34]

$$\mathbf{Y}^{\text{M3}} = \mathbf{W}^{\mathsf{H}}\mathbf{A}(\bar{\boldsymbol{\Theta}})\boldsymbol{\Gamma}(\bar{\boldsymbol{\Theta}}, \beta, \bar{\mathbf{d}}) + \mathbf{N}. \tag{17}$$

Note that M3 is the only model that uses the element pattern model defined in (5). The purpose of this model is to highlight

[7]If UE positions are unknown, calibration (i.e., estimating $\mathbf{W}$ and $\boldsymbol{\Gamma}$) needs to be performed jointly with localization (i.e., estimating $\boldsymbol{\Theta}$). However, this joint problem is non-identifiable, as the observation model is invariant to unitary transformations of the latent factors. For any unitary matrix $\mathbf{D}$, $(\mathbf{DW})^{\mathsf{H}}\mathbf{DA} = \mathbf{W}^{\mathsf{H}}\mathbf{A}$, yielding equivalent observations. With appropriate priors (e.g., a partially calibrated codebook $\mathbf{W}$ or known reference directions), the joint estimation can be reformulated as a Bayesian inference problem, which is left for future work.

the coupling of channel gain and element pattern, and a simple element pattern cannot accurately capture the beam response.

4) Joint Codebook and Gain Matrix Calibration (M4): The most practical model is to estimate $\mathbf{W}$ and nuisance parameters $\mathbf{\Gamma}$ jointly, and the calibration model can be formulated as [22]

$$\mathbf{Y}^{\mathrm{M4}} = \mathbf{W}^{\mathsf{H}}\mathbf{A}(\bar{\mathbf{\Theta}})\mathbf{\Gamma} + \mathbf{N}. \tag{18}$$

Compared with (15) to (16), the introduced unknowns $\mathbf{W}$ and $\mathbf{\Gamma}$ increase the difficulty of the beam calibration task, requiring dedicated calibration algorithms, which will be detailed in Section IV.

E. Calibration Pipeline

To clarify the practical operation of the proposed framework, we summarize the cooperative calibration procedure as follows:

1) Calibration agent association: UEs with reliable location information (e.g., GNSS or high-accuracy positioning) enter the BS coverage area and serve as calibration agents. Upon association, the BS provides the current beam pattern parameters.
2) Sensing-based monitoring: The BS or UEs perform sensing-based angle estimation using the current beam parameters. The estimated angle is compared with the ground-truth angle from BS to UE.
3) Calibration trigger: If the deviation between the estimated angle and the ground-truth location exceeds a predefined threshold, cooperative calibration is triggered.
4) Local data collection and update: Participating UEs collect received beamformed signals and locally update calibration parameters using the proposed loss-based algorithm.
5) Model aggregation at the BS: The locally updated parameters are transmitted to the BS, which aggregates them to update the global calibration model.
6) Beam pattern deployment: The updated beam parameters are used for subsequent sensing and communication beamforming operations.

In practice, calibration errors are typically quasi-static. However, structural changes such as codebook updates, array reconfiguration, or hardware malfunction may invalidate previously calibrated parameters. In such cases, cooperative calibration can be re-triggered. This naturally leads to a two-timescale strategy [35], where calibration and codebook updates operate on a slower, event-driven timescale, while sensing and communication beamforming operate on a faster timescale using the calibrated beam patterns.

In this work, the primary technical focus lies in the local data collection, model aggregation and beam pattern deployment, as shown in Fig. 1, while system-level trigger design and protocol optimization are beyond the scope of this study.

III. Performance Metrics and Loss Functions

This section starts by introducing several performance metrics, namely, response similarity, bias angle error, and codebook gain loss. Then, response error loss and angle error loss will be explained for calibration.

A. Performance Metrics

To evaluate the quality of beam calibration, we introduce beam response similarity, angle estimation error, and codebook gain loss to evaluate the beam pattern error, sensing, and communication performance using the calibrated beams, respectively.

1) Beam Response Similarity: The total variation distance of power angular spectrum is often used to quantify the similarity between the reconstructed beam pattern and the reference one in OTA and channel emulation testing, as defined in 3GPP TR 38.827 [36]. With the reconstructed pattern $\hat{\mathbf{b}}(\boldsymbol{\vartheta})$ and the ground truth $\bar{\mathbf{b}}(\boldsymbol{\vartheta})$, the variation distance of two beam patterns can be defined as

$$\tilde{E}_{\mathrm{R}} = \frac{1}{2}\int_{\boldsymbol{\vartheta}} \left| \frac{|\hat{b}(\boldsymbol{\vartheta})|}{\int_{\boldsymbol{\vartheta}} |\hat{b}(\boldsymbol{\vartheta})| \mathrm{d}\boldsymbol{\vartheta}} - \frac{|\bar{b}(\boldsymbol{\vartheta})|}{\int_{\boldsymbol{\vartheta}} |\bar{b}(\boldsymbol{\vartheta})| \mathrm{d}\boldsymbol{\vartheta}} \right| \mathrm{d}\boldsymbol{\vartheta}. \tag{19}$$

However, the above equation only reflects the gain of the beam pattern (i.e., phase is ignored) and the integral is impractical for the discrete measurements. Based on (19), we define a discrete version of the normalized response error E_{R}. By choosing a set of anchor angles $\mathbf{\Theta}_s = [\boldsymbol{\vartheta}_1, \ldots, \boldsymbol{\vartheta}_S]$ ($S \leq T$ with $\mathbf{\Theta}_s$ as a subset of all the measurement angles $\mathbf{\Theta}$), the response similarity S_{R} ($0 \leq S_{\mathrm{R}} \leq 1$) can be defined as

$$S_{\mathrm{R}} = 1 - E_{\mathrm{R}} = 1 - \frac{1}{2}\left\| \frac{\hat{\mathbf{B}}(\mathbf{\Theta}_s)}{\|\hat{\mathbf{B}}(\mathbf{\Theta}_s)\|_{\mathrm{F}}} - \frac{\bar{\mathbf{B}}(\mathbf{\Theta}_s)}{\|\bar{\mathbf{B}}(\mathbf{\Theta}_s)\|_{\mathrm{F}}} \right\|_{\mathrm{F}}. \tag{20}$$

Here, the response similarity can also be modified by adding different weighting factors for each anchor angle, depending on the area of interest (e.g., large weights for boresight directions). For simplicity, we set identical weights for all measurement angles, yielding (20).

2) Angle Estimation Bias: Although response similarity can be used to evaluate differences between reconstructed beam patterns and ground truth, its performance in angle estimation cannot be directly quantified. To facilitate sensing-based performance evaluation, we adopt a pseudo-true parameter vector, which is defined as the point that minimizes the Kullback-Leibler divergence between $f_{\mathrm{TM}}(\mathbf{y}|\bar{\boldsymbol{\eta}})$ and $f_{\mathrm{MM}}(\mathbf{y}|\boldsymbol{\eta})$ as

$$\boldsymbol{\eta}_0 = \arg\min_{\boldsymbol{\eta}} D_{\mathrm{KL}}(f_{\mathrm{TM}}(\mathbf{y}|\bar{\boldsymbol{\eta}}) \| f_{\mathrm{MM}}(\mathbf{y}|\boldsymbol{\eta})). \tag{21}$$

with $f_{\mathrm{TM}}(\mathbf{y}|\bar{\boldsymbol{\eta}})$ and $f_{\mathrm{MM}}(\mathbf{y}|\boldsymbol{\eta})$ as the probability density functions of the true model and the mismatched model, respectively. The pseudo-true parameter is denoted as $\boldsymbol{\eta}_0 = [\mathrm{Re}(\gamma_0), \mathrm{Im}(\gamma_0), \theta_0^{\mathrm{az}}, \theta_0^{\mathrm{el}}]^{\top}$, containing the nuisance parameter channel gain and the angle estimation. We use this real-valued parameterization to enable standard real-domain differentiation and Fisher-information-based analysis, while retaining the complex gain as a nuisance parameter. The groundtruth state vector and the state variable are denoted as $\bar{\boldsymbol{\eta}}$ and $\boldsymbol{\eta}$.

Specifically, we adopt the ground truth beam pattern measurement $\bar{\mathbf{b}}(\boldsymbol{\vartheta})$ from the chamber as the true model

$$\mathbf{y}_{\mathrm{TM}} = \underbrace{\gamma\bar{\mathbf{b}}(\boldsymbol{\vartheta})}_{=\bar{\boldsymbol{\mu}}(\boldsymbol{\eta})} + \mathbf{n}, \tag{22}$$

and take the calibrated model as the mismatched model

$$\mathbf{y}_{\mathrm{MM}} = \underbrace{\gamma\mathbf{b}(\boldsymbol{\vartheta})}_{=\boldsymbol{\mu}(\boldsymbol{\eta})} + \mathbf{n} = \gamma\mathbf{W}^{\mathsf{H}}\mathbf{a}(\boldsymbol{\vartheta}) + \mathbf{n}, \tag{23}$$

where $\mathbf{y}_{\text{TM}} \sim f_{\text{TM}}(\mathbf{y}|\boldsymbol{\eta})$ and $\mathbf{y}_{\text{MM}} \sim f_{\text{MM}}(\mathbf{y}|\boldsymbol{\eta})$. Note that the pseudo-true parameter reflects the best performance that an estimator can achieve, which is limited by the bias as $\|\boldsymbol{\vartheta}_0 - \bar{\boldsymbol{\vartheta}}\|$. By defining $\boldsymbol{\epsilon}(\boldsymbol{\eta}) \triangleq \bar{\boldsymbol{\mu}}(\bar{\boldsymbol{\eta}}) - \boldsymbol{\mu}(\boldsymbol{\eta})$, the pseudo-true parameter can be obtained as follows [37]:

$$\boldsymbol{\eta}_0 = \arg\min_{\boldsymbol{\eta}} \|\boldsymbol{\epsilon}(\boldsymbol{\eta})\|^2 = \arg\min_{\boldsymbol{\eta}} \|\bar{\boldsymbol{\mu}}(\bar{\boldsymbol{\eta}}) - \boldsymbol{\mu}(\boldsymbol{\eta})\|^2. \quad (24)$$

In (24), $\boldsymbol{\eta}$ includes both the angle $\boldsymbol{\vartheta}$ and the nuisance parameter channel gain α, being consistent with the pseudo-true parameter definition. A practical solution is to estimate $\boldsymbol{\eta}_0$ using gradient-based methods initialized with the true value $\bar{\boldsymbol{\eta}}$ under the assumption that UE positions are known. With the pseudo-true angle estimation $\boldsymbol{\vartheta}_0 = [\theta_0^{\text{az}}, \theta_0^{\text{ele}}]^\top$, we define angle estimation error as

$$\tilde{E}_{\text{A}} = \int_{\boldsymbol{\vartheta}} \|\hat{\boldsymbol{\vartheta}}_{\mathbf{y}_{\text{MM}|\hat{\mathbf{b}}(\cdot)}}(\bar{\mathbf{b}}(\boldsymbol{\vartheta})) - \boldsymbol{\vartheta}\|^2 \mathrm{d}\boldsymbol{\vartheta}, \quad (25)$$

where $\hat{\boldsymbol{\vartheta}}_{\mathbf{y}_{\text{MM}|\hat{\mathbf{b}}(\cdot)}}(\bar{\mathbf{b}}(\boldsymbol{\vartheta})) \triangleq \boldsymbol{\vartheta}_0$ denotes the estimated angle with $\bar{\mathbf{b}}(\boldsymbol{\vartheta})$ as the input and the reconstructed beam pattern $\hat{\mathbf{b}}(\cdot)$ for signal model $\mathbf{y}_{\text{MM}|\hat{\mathbf{b}}(\cdot)}$. Similar to (20), a tractable angle error loss can be defined using a set of anchor angles $\boldsymbol{\Theta}_s = [\boldsymbol{\vartheta}_1, \ldots, \boldsymbol{\vartheta}_S]^\top$ as

$$E_{\text{A}} = \frac{\sum_s \|\hat{\boldsymbol{\vartheta}}_{\mathbf{y}_{\text{MM}|\hat{\mathbf{b}}(\theta)}}(\bar{\mathbf{b}}(\boldsymbol{\vartheta}_s)) - \boldsymbol{\vartheta}_s\|^2}{S}. \quad (26)$$

Here, the angle error E_{A} captures the average angle estimation error using the calibrated beam pattern model to process the data from the true model, which serves as a sensing-oriented performance metric.

3) Codebook Gain Loss: As a benchmark for communication, we define gain loss to quantify the effect of calibration on communication performance in the LOS scenario. Specifically, the best beam is selected based on the known beam pattern to achieve the maximum LOS gain (i.e., ideal beam pattern for the uncalibrated case and M1 to M4 for the calibrated array). Similar to the E_{R} and E_{A}, the gain loss can be expressed as the average relative gain between the BS-assumed beam pattern and the ideal beam pattern among all the anchor angles

$$E_{\text{C}} = \frac{1}{S}\sum_s \frac{\left\|\bar{\mathbf{b}}_{\hat{g}_s^\star}^{\mathsf{H}}(\boldsymbol{\vartheta}_s)\mathbf{a}(\boldsymbol{\vartheta}_s)\right\|^2}{\left\|\tilde{\mathbf{b}}_{\tilde{g}_s^\star}^{\mathsf{H}}(\boldsymbol{\vartheta}_s)\mathbf{a}(\boldsymbol{\vartheta}_s)\right\|^2}. \quad (27)$$

where $\hat{g}_s^\star = \arg\max_g |\hat{\mathbf{b}}_g(\boldsymbol{\vartheta}_s)|$ and $\tilde{g}_s^\star = \arg\max_g |\tilde{\mathbf{b}}_g(\boldsymbol{\vartheta}_s)|$ are the optimal beam indices obtained from the calibrated beam pattern $\hat{\mathbf{b}}(\boldsymbol{\vartheta})$ and the ideal beam pattern $\tilde{\mathbf{b}}(\boldsymbol{\vartheta})$ defined in (4), respectively. The communication gain loss in (27) is computed as the ratio between the achieved beamforming gain and the ideal gain (i.e., using M1), reported in dB scale. This expression reflects the effective beamforming gain in the communication direction, which determines the received SNR and achievable rate. Calibration errors distort the beam pattern and reduce the beamforming gain, thereby degrading communication performance. This degradation will be evaluated via simulations in Sec. V.

Nevertheless, the primary focus of this work is sensing-based calibration. A fully joint ISAC-oriented calibration framework that explicitly balances sensing and communication metrics is beyond the current scope and will be considered in future work.

B. Loss Functions

1) Response Error Loss: Inspired by the response similarity defined in (20), we aim to reduce the error between the reconstructed beam pattern and the reference one, and formulate the response error loss (REL)-based calibration. Given the received signal $\mathbf{Y}$, the calibration task is to find the optimal $\mathbf{W}$ and $\boldsymbol{\Gamma}$ that minimize the REL L_{REL} as

$$[\hat{\mathbf{W}}, \hat{\boldsymbol{\Gamma}}] = \arg\min_{\mathbf{W},\boldsymbol{\Gamma}} \; L_{\text{R}}(\mathbf{Y}, \mathbf{W}, \boldsymbol{\Gamma}), \quad \text{s.t.} \|\mathbf{w}_g\|_2 = 1, \; \forall g, \quad (28)$$

where

$$L_{\text{R}}(\mathbf{Y}, \mathbf{W}, \boldsymbol{\Gamma}) = \frac{1}{T}\|\mathbf{Y} - \mathbf{W}^{\mathsf{H}}\mathbf{A}\boldsymbol{\Gamma}\|_{\text{F}}^2. \quad (29)$$

The above formulation can be implemented for both 2D and 3D beams, with each column of $\mathbf{A}$ representing a steering vector for a specific target position. Physically, L_R enforces beam-pattern fidelity by minimizing the reconstruction error between the calibrated model and the measurements.

2) Angle Error Loss: Based on the definition of angle error in (26), we can formulate angle error loss (AEL) as

$$\tilde{L}_{\text{A}}(\mathbf{Y}, \mathbf{W}, \boldsymbol{\Gamma}) = \frac{1}{T}\sum_{t=1}^{T} \|\hat{\boldsymbol{\vartheta}}_{\mathbf{y}_{\text{MM}|\hat{\mathbf{b}}(\boldsymbol{\vartheta})}}(\mathbf{y}_t) - \boldsymbol{\vartheta}_t\|^2. \quad (30)$$

Equation (30) is conceptually aligned with the sensing objective, since it penalizes the deviation between the angle estimate produced by the calibrated model and the known reference angle. However, this loss function requires bilevel optimization [38], where an inner optimization (i.e., finding the pseudo-true angle) needs to be solved to calculate the loss values. To assist calibration, we propose a differentiable AEL function to reduce sensing angle error.

To obtain a tractable surrogate, we use the fact that the angle estimator in (12) is based on the normalized projection magnitude

$$\frac{|\mathbf{b}^{\mathsf{H}}(\boldsymbol{\vartheta})\mathbf{y}|}{\|\mathbf{b}(\boldsymbol{\vartheta})\|}.$$

Hence, a natural proxy for reducing the angle error in (30) is to align these normalized projection responses at the anchor angles $\boldsymbol{\Theta}_s$. If the true beam response $\bar{\mathbf{b}}(\boldsymbol{\vartheta})$ were available, one would minimize

$$\left(\frac{|\mathbf{b}^{\mathsf{H}}(\boldsymbol{\vartheta}_t)\mathbf{y}_s|}{\|\mathbf{b}(\boldsymbol{\vartheta}_t)\|} - \frac{|\bar{\mathbf{b}}^{\mathsf{H}}(\boldsymbol{\vartheta}_t)\mathbf{y}_s|}{\|\bar{\mathbf{b}}(\boldsymbol{\vartheta}_t)\|}\right)^2,$$

for measurement index t and anchor index s.

In practice, however, the true beam response $\bar{\mathbf{b}}(\boldsymbol{\vartheta})$ is unknown, while the received signals are observed. We therefore replace the inaccessible reference projection by the measurement vector $\mathbf{y}_t$, which yields the surrogate

$$\tilde{L}_A = \frac{1}{TS}\sum_{t,s}\left(\frac{|\mathbf{b}^{\mathsf{H}}(\boldsymbol{\vartheta}_t)\mathbf{y}_s|}{\|\mathbf{b}(\boldsymbol{\vartheta}_t)\|} - \frac{|\mathbf{y}_t^{\mathsf{H}}\mathbf{y}_s|}{\|\mathbf{y}_t\|}\right)^2. \quad (31)$$

This loss matches normalized projection magnitudes across the anchor angles. Since the angle estimator in (12) selects the

angle corresponding to the maximum normalized projection response, mismatches in these projections may shift the peak location of the projection function and thereby introduce angle estimation bias. By aligning the normalized projections at the reference angles, the surrogate loss reduces such peak shifts and thus helps reduce the resulting angle error. The following lemma shows that the proposed surrogate loss is consistent under ideal noise-free conditions.

Lemma 1 (Consistency of the magnitude-based surrogate): Suppose the calibrated beam response matches the true beam response at the reference angles, i.e., $\mathbf{b}(\boldsymbol{\vartheta}_t) = \bar{\mathbf{b}}(\boldsymbol{\vartheta}_t), \forall t$. Then every term in (31) is zero under noise-free conditions, and hence $\tilde{L}_A = 0$.

Proof: Under the assumption of matching beam responses, $|\mathbf{b}^{\mathsf{H}}(\boldsymbol{\vartheta}_t)\mathbf{y}_s|/\|\mathbf{b}(\boldsymbol{\vartheta}_t)\| = |\bar{\mathbf{b}}^{\mathsf{H}}(\boldsymbol{\vartheta}_t)\mathbf{y}_s|/\|\bar{\mathbf{b}}(\boldsymbol{\vartheta}_t)\|$. Moreover, since under noise-free conditions $\mathbf{y}_t = \alpha_t \bar{\mathbf{b}}(\boldsymbol{\vartheta}_t)$,

$$\frac{|\mathbf{y}_t^{\mathsf{H}}\mathbf{y}_s|}{\|\mathbf{y}_t\|} = \frac{|\alpha_t^* \bar{\mathbf{b}}^{\mathsf{H}}(\boldsymbol{\vartheta}_t)\mathbf{y}_s|}{|\alpha_t|\|\bar{\mathbf{b}}(\boldsymbol{\vartheta}_t)\|} = \frac{|\bar{\mathbf{b}}^{\mathsf{H}}(\boldsymbol{\vartheta}_t)\mathbf{y}_s|}{\|\bar{\mathbf{b}}(\boldsymbol{\vartheta}_t)\|}.$$

Hence, the two terms inside each summand of (31) are equal, so every summand is zero.□

For optimization, we further replace magnitude matching in (31) by complex projection matching and adopt the differentiable loss

$$L_{\mathrm{A}}(\mathbf{Y}, \mathbf{W}, \boldsymbol{\Gamma}) = \frac{1}{TS}\sum_{t,s} |e_{t,s}|^2,$$

$$e_{t,s} = u_{t,s} - \breve{u}_{t,s} = \frac{\mathbf{b}^{\mathsf{H}}(\boldsymbol{\vartheta}_t)\mathbf{y}_s}{\|\mathbf{b}(\boldsymbol{\vartheta}_t)\|} - \frac{\mathbf{y}_t^{\mathsf{H}}\mathbf{y}_s}{\|\mathbf{y}_t\|}. \quad (32)$$

Here, $\mathbf{b}(\boldsymbol{\vartheta}) = \gamma(\boldsymbol{\vartheta})\mathbf{W}^{\mathsf{H}}\mathbf{a}(\boldsymbol{\vartheta})$ denotes the calibrated beam pattern, and $\mathbf{y}_t$ and $\mathbf{y}_s$ are the received signal at the $\boldsymbol{\vartheta}_t$ and $\boldsymbol{\vartheta}_s$, respectively. The term $\breve{u}_{t,s}$ is defined by replacing $\bar{\mathbf{b}}(\boldsymbol{\vartheta}_t)$ in $\frac{\bar{\mathbf{b}}^{\mathsf{H}}(\boldsymbol{\vartheta}_t)\mathbf{y}_s}{\|\mathbf{b}(\boldsymbol{\vartheta}_t)\|}$ with a noisy measurement $\mathbf{y}_t$ for practical implementation purposes. The loss function L_A promotes accurate angle estimation by aligning normalized projections across anchor angles, which reduces peak shifts in the projection response caused by beam distortions. Matching complex projections is a stronger condition than matching their magnitudes. In particular, if $u_{t,s} = \breve{u}_{t,s}$, then $|u_{t,s}| = |\breve{u}_{t,s}|$, implying that minimizing (32) promotes the magnitude consistency required by (31). Moreover, since the angle estimator in (12) depends only on the projection magnitude, the complex formulation serves as a convenient differentiable surrogate without introducing additional phase sensitivity in the angle estimation objective. The overall calibration problem remains nonconvex due to the beamforming parameters, and the complex formulation does not fundamentally alter the nonconvex landscape, but instead provides a smooth objective suitable for gradient-based optimization.

The following lemma establishes that complex projection matching in (32) implies the magnitude-based matching in (31).

Lemma 2: (Complex matching implies magnitude matching): If $L_A = 0$ in (32), then $\tilde{L}_A = 0$ in (31).

Proof: If $L_A = 0$, then $e_{t,s} = 0$ for all t, s, i.e., $\mathbf{b}^{\mathsf{H}}(\boldsymbol{\vartheta}_t)\mathbf{y}_s/\|\mathbf{b}(\boldsymbol{\vartheta}_t)\| = \mathbf{y}_t^{\mathsf{H}}\mathbf{y}_s/\|\mathbf{y}_t\|$. Taking magnitudes on both sides gives $|\mathbf{b}^{\mathsf{H}}(\boldsymbol{\vartheta}_t)\mathbf{y}_s|/\|\mathbf{b}(\boldsymbol{\vartheta}_t)\| = |\mathbf{y}_t^{\mathsf{H}}\mathbf{y}_s|/\|\mathbf{y}_t\|$, for all t, s. Therefore every summand in (31) is zero, which implies $\tilde{L}_A = 0$. □

Finally, similar to (20), the anchor angles[8] $\boldsymbol{\Theta}_s = [\boldsymbol{\vartheta}_1, \ldots, \boldsymbol{\vartheta}_S]^\top$ are chosen as a subset of the measurement angles $\boldsymbol{\Theta} = [\boldsymbol{\vartheta}_1, \ldots, \boldsymbol{\vartheta}_T]^\top$ to reduce the computational complexity while preserving cross-angle consistency in the normalized projections.

IV. Calibration Algorithms

In this section, we start with the REL-based calibration algorithm for model M4 using alternating optimization (AO). Then, REL-based and AEL-based calibration algorithms using gradient descent (GD) will be detailed, followed by the discussions on cooperative strategies and complexity analysis. The calibration using models M1-M3 can be performed as a subproblem of model M4-based calibration, with the knowledge of beamforming angle (M2) and element pattern (M3) that can be obtained from the chamber.

A. REL-Based Calibration (AO)

The idea of AO is to optimize one variable while fixing the other one. We start with the most general case (i.e., M4), where both the beamforming matrix $\mathbf{W}$ and the channel gain matrix $\boldsymbol{\Gamma}$ need to be estimated jointly. For simplicity, the angle set $\boldsymbol{\Theta}$ in (13) is ignored (i.e., using $\mathbf{A}$ instead of $\mathbf{A}(\boldsymbol{\Theta})$), and we set $\rho_s = 1$ for all the sample angles.

1) Update $\boldsymbol{\Gamma}$ Given $\hat{\mathbf{W}}$: A practical way of initializing AO is to use the beamforming direction $\bar{\boldsymbol{\Phi}}$ given by the antenna array manufacturer (see M1 in (15)). With an estimated $\hat{\mathbf{W}}$, the update on $\boldsymbol{\Gamma}$ is straightforward, which can be formulated as

$$\hat{\boldsymbol{\Gamma}} = \arg\min_{\boldsymbol{\Gamma}} \|\mathbf{Y} - \hat{\mathbf{W}}^{\mathsf{H}}\mathbf{A}\boldsymbol{\Gamma}\|_{\mathrm{F}}^2. \quad (33)$$

Since $\boldsymbol{\Gamma}$ is diagonal, each diagonal element γ_t can be updated independently and in parallel as

$$\hat{\gamma}_t = \arg\min_{\gamma} \|\mathbf{y}_t - \gamma\hat{\mathbf{b}}_t\|^2, \quad (34)$$

where $\mathbf{y}_t \in \mathbb{C}^{G\times 1}$ and $\hat{\mathbf{b}}_t$ are the t-th columns of matrices $\mathbf{Y}$ and $\hat{\mathbf{W}}^{\mathsf{H}}\mathbf{A}$, respectively. The closed-form solution is then given by

$$\hat{\gamma}_t = \frac{\hat{\mathbf{b}}_t^{\mathsf{H}}\mathbf{y}_t}{\hat{\mathbf{b}}_t^{\mathsf{H}}\hat{\mathbf{b}}_t}. \quad (35)$$

2) Update $\mathbf{W}$ Given $\hat{\boldsymbol{\Gamma}}$: With a known $\hat{\boldsymbol{\Gamma}}$, the update of $\mathbf{W}$ under the unit-norm constraint on each column can be formulated as

$$\min_{\|\mathbf{w}_g\|_2=1} \|\mathbf{y}_g - \mathbf{w}_g^{\mathsf{H}}\mathbf{A}\hat{\boldsymbol{\Gamma}}\|^2, \quad (36)$$

[8]The set $\boldsymbol{\Theta}_s$ serves as a representative angular basis rather than an arbitrary sampling mechanism. Its purpose is to preserve cross-angle projection consistency while reducing computational complexity. When selecting anchor angles, $\boldsymbol{\Theta}_s$ should cover the angular region of interest and ensure sufficient geometric diversity to improve identifiability. Additionally, a small fraction of boundary angles could be included to improve robustness near angular limits. Finally, if available, extremely low-SNR directions may be excluded to prevent unstable calibration processes.

where $\mathbf{y}_g$ denotes the g-th row of $\mathbf{Y}$. Let $\mathbf{B} = \mathbf{A}\hat{\mathbf{\Gamma}}$, $\mathbf{Q} = \mathbf{B}\mathbf{B}^{\mathsf{H}}$ (Hermitian psd), and $\mathbf{b}_g = \mathbf{B}\mathbf{y}_g^{\mathsf{H}}$. The Karush–Kuhn–Tucker (KKT) optimality conditions for (36) (using Wirtinger calculus for complex variables [39], and the trust-region form [40]) yield the following system:

$$(\mathbf{Q} + \lambda_g \mathbf{I})\mathbf{w}_g = \mathbf{b}_g, \qquad \|\mathbf{w}_g\| = 1, \tag{37}$$

where $\lambda_g \in \mathbb{R}$ is the Lagrange multiplier. The function $f(\lambda_g) = \|(\mathbf{Q} + \lambda_g \mathbf{I})^{-1}\mathbf{b}_g\|$ is strictly decreasing in λ_g. If the least-squares solution $\mathbf{w}_g^{\dagger} = \mathbf{Q}^{\dagger}\mathbf{b}_g$ satisfies $\|\mathbf{w}_g^{\dagger}\|_2 \leq 1$, then it already meets the constraint and the optimum is $\mathbf{w}_g^{\star} = \mathbf{w}_g^{\dagger}$ (i.e., $\lambda_g^{\star} = 0$). Otherwise, its root $\lambda_g^{\star}$ satisfying $f(\lambda_g) = 1$ can be found efficiently via a one-dimensional bisection search. Consequently, the resulting vector $\mathbf{w}_g^{\star} = (\mathbf{Q} + \lambda_g^{\star}\mathbf{I})^{-1}\mathbf{b}_g$ satisfies the unit-norm constraint $\|\mathbf{w}_g^{\star}\|_2 = 1$ and provides the exact constrained minimizer of (36).

B. REL-Based Calibration (GD)

The trust-region formulation in (37) guarantees KKT optimality. However, it incurs a high computational cost since each column $\mathbf{w}_g$ requires solving a scalar root-finding problem involving the matrix inverse $(\mathbf{Q} + \lambda_g \mathbf{I})^{-1}$. This subsection provides a GD-based solution for REL-based calibration with a batch size S_{batch}. Considering the real-valued loss function defined in (20) and its involved complex variables, we develop a gradient-based method to update $\mathbf{W}$ and $\boldsymbol{\gamma}$ based on complex gradient operators [39] (Theorem 4). Specifically, the codebook $\mathbf{W}$ and the channel gain vector $\boldsymbol{\gamma}$ for each iteration are updated with a learning rate l_r as

$$\mathbf{W}^{(i+1)} = \mathbf{W}^{(i)} - l_r \frac{\partial L_{\mathrm{R}}}{\partial \mathbf{W}^*}\bigg|_{\mathbf{W}=\mathbf{W}^{(i)}}, \tag{38}$$

$$\boldsymbol{\gamma}^{(i+1)} = \boldsymbol{\gamma}^{(i)} - l_r \frac{\partial L_{\mathrm{R}}}{\partial \boldsymbol{\gamma}^*}\bigg|_{\boldsymbol{\gamma}=\boldsymbol{\gamma}^{(i)}}. \tag{39}$$

Note that the calculation of $\mathbf{W}^{(i+1)}$ in (38) is followed by the normalization of each codeword to fulfill the constraint. For REL-based calibration, we need to calculate the gradient term $\partial L_{\mathrm{R}}/\partial \mathbf{W}^*$. Based on (29), we can define the residual

$$\mathbf{e}_t = \mathbf{y}_t - \mathbf{b}_t = \mathbf{y}_t - \gamma_t \mathbf{W}^{\mathsf{H}}\mathbf{a}_t, \tag{40}$$

where $\check{\mathbf{b}}_t$, $\mathbf{b}_t$ and $\mathbf{a}_t$ are defined after (45). Expanding the squared norm, we get

$$\begin{aligned}&\|\mathbf{e}_t\|^2 \\ &= \mathbf{y}_t^{\mathsf{H}}\mathbf{y}_t - \mathbf{y}_t^{\mathsf{H}}\gamma_t \mathbf{W}^{\mathsf{H}}\mathbf{a}_t - \gamma_t^* \mathbf{a}_t^{\mathsf{H}}\mathbf{W}\mathbf{y}_t + |\gamma_t|^2 \mathbf{a}_t^{\mathsf{H}}\mathbf{W}\mathbf{W}^{\mathsf{H}}\mathbf{a}_t.\end{aligned} \tag{41}$$

And the gradient of L_{R} with respect to $\mathbf{W}^*$ and γ_t can be expressed respectively as

$$\frac{\partial L_{\mathrm{R}}}{\partial \mathbf{W}^*} = \frac{1}{T}\sum_{t=1}^{T}\left(-\gamma_t \mathbf{a}_t \mathbf{y}_t^{\mathsf{H}} + |\gamma_t|^2 \mathbf{a}_t \mathbf{a}_t^{\mathsf{H}}\mathbf{W}\right), \tag{42}$$

$$\frac{\partial L_{\mathrm{R}}}{\partial \gamma_t^*} = \frac{1}{T}(-\mathbf{a}_t^{\mathsf{H}}\mathbf{W}\mathbf{y}_t + \gamma_t \mathbf{a}_t^{\mathsf{H}}\mathbf{W}\mathbf{W}^{\mathsf{H}}\mathbf{a}_t). \tag{43}$$

Note that the GD-based update on $\boldsymbol{\gamma}$ is not mandatory. By insterting the updated codebook $\hat{\mathbf{W}} = \mathbf{W} - l_r \frac{\partial L_{\mathrm{R}}}{\partial \mathbf{W}^*}$ into (33) with column normalization, AO-based update on the gain matrix $\mathbf{\Gamma}$ can still be performed for REL-based calibration. In the simulation section that follows, we will keep the best-performing method (GD-based update on $\mathbf{W}$ only) and show how mini-batch GD empirically outperforms AO and how the hyperparameters affect the calibration performance.

C. AEL-Based Calibration

Based on the available estimated $\mathbf{W}$, $\mathbf{\Gamma}$ (e.g., from REL-based calibration), the current beam response can be calculated as $\mathbf{B} = \mathbf{W}^{\mathsf{H}}\mathbf{A}(\boldsymbol{\theta})\mathbf{\Gamma}$. Together with the normalized measurement $\check{\mathbf{B}}$, the iterative optimization can be performed for AEL-based calibration for M4 using the loss function L_{A}.

To assist derivation, we compute the gradients of the proposed error loss L_{A} with respect to the model parameters $\mathbf{W}^*$ and γ_t^* using Wirtinger calculus, by calculating the derivative of the loss $e_{t,s}$ with respect to the unknown parameters and summing over T samples and S anchors. The gradients of the proposed error loss L_{DA} with respect to the model parameters $\mathbf{W}^*$ and γ_t^* are given by

$$\frac{\partial L_{\mathrm{A}}}{\partial \mathbf{W}^*} = \frac{\sum_{t,s}\left[\frac{\gamma_t}{q_t}\, e_{t,s}\, \mathbf{a}_t \mathbf{y}_s^{\mathsf{H}} - \frac{|\gamma_t|^2}{q_t^2}\, \Re\{e_{t,s} u_{t,s}^*\}\, \mathbf{a}_t \mathbf{a}_t^{\mathsf{H}}\mathbf{W}\right]}{TS}, \tag{44}$$

$$\frac{\partial L_{\mathrm{A}}}{\partial \gamma_t^*} = \frac{j\sum_s \rho_{t,s}\, \Im\{e_{t,s}^* u_{t,s}\}}{\gamma_t^* TS}. \tag{45}$$

The intermediate variables are defined as $\mathbf{a}_t = \mathbf{a}(\vartheta_t)$, $q_t = |\gamma_t|\|\mathbf{W}^{\mathsf{H}}\mathbf{a}_t\|$, $p_{t,s} = \gamma_t \mathbf{a}_t^{\mathsf{H}}\mathbf{W}\mathbf{y}_s$, $u_{t,s} = \frac{p_{t,s}}{q_t}$, $\check{u}_{t,s} = \frac{\mathbf{y}_t^{\mathsf{H}}\mathbf{y}_s}{\|\mathbf{y}_t\|}$. The AEL-based calibration is based on the loss function in (32) and hence there is no closed-form solution for γ_t, in contrast to the REL-based calibration in (35). The detailed derivation is provided in Appendix A.

D. Convergence Analysis

The calibration problems underlying REL-AO, REL-GD, and AEL are nonconvex due to the bilinear coupling between $\mathbf{W}$ and $\mathbf{\Gamma}$ and the nonlinear beam response structure. Hence, global optimality cannot be guaranteed. Nevertheless, convergence to first-order stationary points can be established under standard smooth optimization assumptions.

1) Convergence of REL-AO: REL-AO alternately minimizes $L_R(\mathbf{W}, \mathbf{\Gamma})$ with respect to $\mathbf{\Gamma}$ and $\mathbf{W}$. For fixed $\mathbf{W}$, the update of $\mathbf{\Gamma}$ in (33) yields the exact global minimizer of a convex quadratic problem. For fixed $\mathbf{\Gamma}$, each $\mathbf{w}_g$ is obtained by solving the trust-region subproblem in (36) exactly via its Karush–Kuhn–Tucker (KKT) conditions. Thus, every block update produces a nonincreasing objective value. Since $L_R(\mathbf{W}, \mathbf{\Gamma})$ is continuously differentiable and bounded below, and each column of $\mathbf{W}$ is constrained to lie on the unit sphere, the feasible set for $\mathbf{W}$ is compact. Moreover, for any fixed $\mathbf{W}$, the least-squares update of $\mathbf{\Gamma}$ admits a unique minimizer, so the iterates remain bounded through their dependence on $\mathbf{W}$. Under these conditions, the alternating scheme constitutes an exact block coordinate descent method with exact minimization per block. Therefore, every limit point generated by REL-AO is a first-order stationary point of the REL problem [41, Prop. 2.7.1].

2) Convergence of REL-GD: The REL objective is continuously differentiable with Lipschitz-continuous gradient (being quadratic in $(\mathbf{W}, \mathbf{\Gamma})$). The update in (38) follows the negative gradient direction with constant step size $l_r > 0$, and normalizing each column of $\mathbf{W}$ after every update corresponds to a projection onto the product of unit spheres, ensuring that the iterates remain in a compact feasible set. Hence, the method can be interpreted as projected gradient descent on a smooth objective over a compact constraint set. Under these conditions, any sufficiently small constant step size l_r (see the step-size condition in [41, Prop. 1.2.3]) ensures that every limit point of the generated sequence is a first-order stationary point of the REL problem.

3) Convergence of AEL-Based Calibration: The AEL surrogate loss in (32) is continuously differentiable (excluding degenerate points where $\gamma_t = 0$ or $\|\mathbf{W}^{\mathsf{H}}\mathbf{a}_t\| = 0$) and has Lipschitz-continuous gradient over bounded feasible sets that are bounded away from such degeneracies. The update also follows the negative gradient direction with constant step size $l_r > 0$, and normalization keeps the iterates bounded. Therefore, under the same projected gradient framework and for sufficiently small constant step size l_r, the iterates converge to first-order stationary points of the AEL problem [41, Prop. 1.2.3]. Due to the more involved nonlinear structure of the projection-matching formulation, the AEL objective may contain additional local minima compared to REL, resulting in stronger sensitivity to initialization as observed in simulations.

E. Implementation Details

Note that all proposed iterative calibration methods (REL-AO, REL-GD, and AEL) follow a unified stopping rule. The algorithm terminates when the relative decrease of the objective function satisfies $\frac{|L^{(k)}-L^{(k-1)}|}{L^{(k-1)}} < \epsilon$ (e.g., ϵ_{rel-ao}, ϵ_{rel-gd}, and ϵ_{ael} for three calibration methods), or when a predefined maximum number of iterations $I_{\max}$ (e.g., $I_{\max,rel-ao}$, $I_{\max,rel-gd}$, and $I_{\max,ael}$) is reached. However, the calibration performance is affected by the parameter selections, as will be shown in Sec. V. Different initialization strategies have been adopted for the discussed methods to ensure stable optimization. Specifically, REL-AO was initialized using the nominal (uncalibrated) beam pattern parameters. Then, the converged result of this method was used to initialize REL-GD, allowing GD to further refine the solution. In addition, the AEL-based method was initialized using the REL-GD output, serving as a sensing-oriented refinement stage. This hierarchical initialization improves stability and ensures fair comparison among the optimization variants.

F. Cooperative Calibration

From the calibration models, we can see that the channel gain matrix is only used for beam representation, which aligns the reconstructed beam pattern as closely as the original ground truth pattern. When performing localization and sensing, the complex gain will be a function of the target angle and the codebook, as shown in equation (11). Consequently, the matrix $\mathbf{W}$ is the variable of interest for calibration.

Ideally, the BS can collect all the received signals from several UEs, and calibration can be done centrally based on the ground truth UE state. In the centralized formulation, all UEs transmit their measurements to the BS for joint parameter optimization. The update involves matrix operations whose dimension scales with the total number of UEs and calibration parameters. As a result, both computational complexity and memory usage at the BS increase with network size. Instead, UEs transmit locally updated model parameters rather than raw measurement data to the BS in the distributed framework. Hence, the communication overhead scales with the number of calibration parameters rather than the number of snapshots or antennas. When each UE collects many snapshots, this substantially reduces the communication load compared to centralized raw data transmission. By using a federated learning strategy initialized with a local model broadcast by the BS as $\mathbf{W}^-$, each user m can update the local model with the beam pattern difference $\Delta_{\mathbf{W}_m}$, and the BS can aggregate the local models as

$$\mathbf{W}^+ = \mathbf{W}^- + \sum_m \xi_m \Delta_{\mathbf{W}_m}, \tag{46}$$

where ξ_m is the weighting coefficient for the m-th local model. While the choice of coefficients (e.g., based on the UE's hardware capability, location, and number of measurements) influences performance, this work focuses on evaluation rather than on their optimization. In the above equation, the nuisance parameter $\mathbf{\Gamma}_m$ is not included and the beamforming matrix $\mathbf{W}^+$ also needs to be normalized after each update. However, it could be utilized to design the weighting coefficients (e.g., larger coefficients for the model with a larger channel gain).

It should be noted that the distributed implementation may incur a performance gap compared to fully centralized optimization, since centralized processing has access to globally aggregated data and can jointly optimize all parameters. The distributed scheme trades potential optimality for improved scalability and reduced per-node computational burden. The magnitude of this gap depends on many factors, such as dataset selection and calibration approach.

G. Complexity Analysis

The computational complexity of the proposed calibration methods is analyzed as follows. For REL-based calibration with AO, the update of $\mathbf{\Gamma}$ in (33) requires matrix multiplication with complexity cost as $\mathcal{O}(GNT)$. The update of $\mathbf{W}$ in (36) requires $\mathcal{O}(GNT + N^2T + GN^2)$ operations for matrix multiplication, followed by eigen decomposition and bisection search with the complexity of $\mathcal{O}(N^3)$ and $\mathcal{O}(LGN^2)$, respectively. Therefore, the total computational complexity per iteration is $\mathcal{O}\big(GNT+N^2T+GN^2+N^3+LGN^2\big)$. For REL-based calibration using GD in (42), the gradient evaluation can be efficiently implemented via rank-one updates, resulting in a per-sample cost of $\mathcal{O}(GN)$ and hence $\mathcal{O}(GNT_b)$ per iteration with batch size T_b. Since calibration is event-driven rather than continuously repeated, only a limited number of aggregation rounds are required when recalibration is triggered. For AEL-based calibration in (44) and (45), evaluating the gradient requires computing $a_s^{\mathsf{H}}\mathbf{W}$ once per sample at cost $\mathcal{O}(NG)$, and then accumulating across T_b samples and S anchors, resulting in a complexity of $\mathcal{O}(GNT_bS)$. The number of

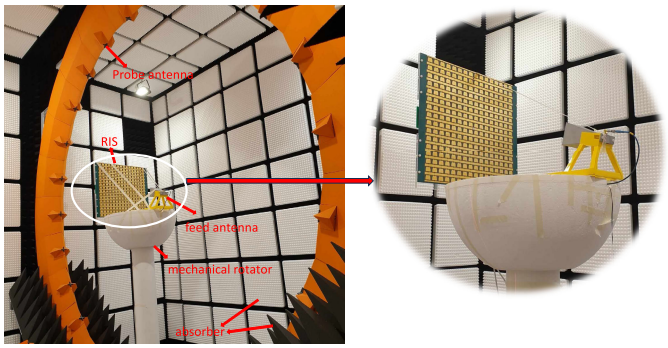

Fig. 2. The photo of the RIS pattern measurements in the anechoic chamber .

anchors S introduces a bias–complexity tradeoff. If S is too small, insufficient angular coverage may leave certain regions underconstrained, increasing angle bias. Increasing S improves robustness and reduces approximation error at the cost of linearly increased computation.

In summary, REL-based calibration using GD scales linearly with the batch size and the number of antennas and anchors, providing a flexible and robust solution towards calibration. On the one hand, it is flexible in that it can be applied to different array sizes, geometries, and beam codebooks without requiring structural modification of the algorithm. On the other hand, it is robust because it does not rely on a specific hardware impairment model, but instead calibrates the effective beam pattern resulting from all underlying distortions. Besides, the proposed calibration method does not require direct access to or control over individual element excitations. The calibration procedure can be performed while the BS operates under its default beamforming configurations, relying solely on the observed beam responses. In addition, we notice that the AEL-based algorithm has a higher complexity than the REL-based calibration, depending on the anchor size S.

V. Simulation and Experimental Validation

We start with the measurement data from the chamber, which serves two purposes: (i) to provide ideal measured data to evaluate different beam pattern models, and (ii) to benchmark the developed calibration algorithms in more practical settings (e.g., different transmit powers). However, the proposed cooperative calibration can also be applied in practical scenarios. In addition, both 2D and 3D beam pattern calibration results will be presented, and different calibration scenarios will also be evaluated.

A. System Setup

To obtain the ground truth calibration data, we measured the reflected beam pattern of a real-world RIS plate[9] in the anechoic chamber, as shown in Fig. 2. The specifications of the RIS board under test are summarized in Table II, and more details on its design can be found in [44]. The adopted RIS prototype consists of a programmable 16×16 element array. From a beam-pattern calibration perspective, it exhibits several characteristics that are common across antenna array architectures, including (i) large-aperture beamforming behavior, (ii) directional beam scanning using a predefined codebook, and (iii) practical hardware imperfections that lead to measurable deviations between ideal and measured beam patterns. In each beam, RIS coefficients can be programmed to assign the phase shift values to maximize the energy in this direction, and the corresponding beam pattern requires calibration.

TABLE II
RIS Specifications and Calibration Parameters

Parameters	2D	3D
Operation frequency	5 GHz	
Phase-shifter resolution	2-bit (0°, 90°, 180° and 270°)	
Polarization	linear polarization	
G (beams)	11	66
N (antennas)	16	256
T (sample angles)	561	12831
Sample angle range (azi.)	$[-70°, 70°]$	$[-70°, 70°]$
Sample angle range (ele.)	-	$[-70°, 20°]$
S (anchor angles)	81	119
Anchor angle range (azi.)	$[-40°, 40°]$	$[-40°, 40°]$
Anchor angle range (ele.)	-	$[-40°, 10°]$
M (cooperative users)	3	-
$l_{r\mathrm{R}}$, $l_{r\mathrm{A}}$: learning rate	0.02, 0.03	0.1, 0.2
$I_{\text{rel-ao}}$, $I_{\text{rel-gd}}$, I_{ael}: Max iterations	100, 100, 200	10, 10, 10
$\epsilon_{\text{rel-ao}}$, $\epsilon_{\text{rel-gd}}$, ϵ_{ael}: Stop threshold	1e-6, 1e-6, 1e-8	1e-6, 1e-6, 1e-8

Here, we measured $G = 6 \times 11 = 66$ beam patterns with its target boresight direction pointing at $\bar{\mathbf{\Phi}} = [\bar{\phi}^{\mathrm{az}}, \bar{\phi}^{\mathrm{el}}]^\top$ where $\bar{\phi}^{\mathrm{az}} \in \{-50°, -40°, \ldots, 50°\}$, $\bar{\phi}^{\mathrm{el}} \in \{-50°, -40°, \ldots, 0°\}$, respectively. The sampling angle range is dictated by the available measurement data, whereas the anchor angle range is selected according to the angular sector of practical interest, where the majority of the beam energy is concentrated. The SNR of the measurements in the chamber was around 35 dB. Note that the boresight direction of the practical RIS beams can be different from the target angles, which is one of the key motivations for beam calibration. The resulting beam patterns were measured over a hemispherical range, with the azimuth angle varying from $-90°$ to $90°$ and the elevation angle from $-90°$ to $90°$, both sampled at $1°$ intervals, resulting in a measurement dataset $\bar{\mathbf{B}}_{\mathrm{3D}} \in \mathbb{C}^{66\times 181\times 181}$. For 2D beam pattern calibration, we set the elevation angle as $0°$ and use a subset of the measurement data as $\bar{\mathbf{B}}_{\mathrm{2D}} \in \mathbb{C}^{11\times 181}$. The measurement data is used as the ground truth and for generating synthetic measurement data for calibration performance evaluation in different scenarios.

B. Visualization of Measurement Data

The visualization of a specific 3D codeword (beamforming direction $[0°, 0°]^\top$) can be found in Fig. 3 (a). When considering 2D beam pattern calibration, the beam patterns of 11 codewords are shown in Fig. 3 (b). For better visualization

[9]In this work, the measured RIS reflective beam patterns (e.g., in an RIS-integrated BS [42], [43]) are employed to validate the proposed beam model and to serve as ground-truth calibration data. This is motivated by the current lack of comprehensive measured beam pattern datasets for large-scale antenna arrays that cover a wide range of steering directions. Using RIS measurements as a substitute is reasonable as both structures exhibit similar array-level non-idealities, including mutual coupling, element pattern distortions, and non-ideal phase tuning or excitation errors. These factors influence the beam response in a mathematically analogous manner for both systems.

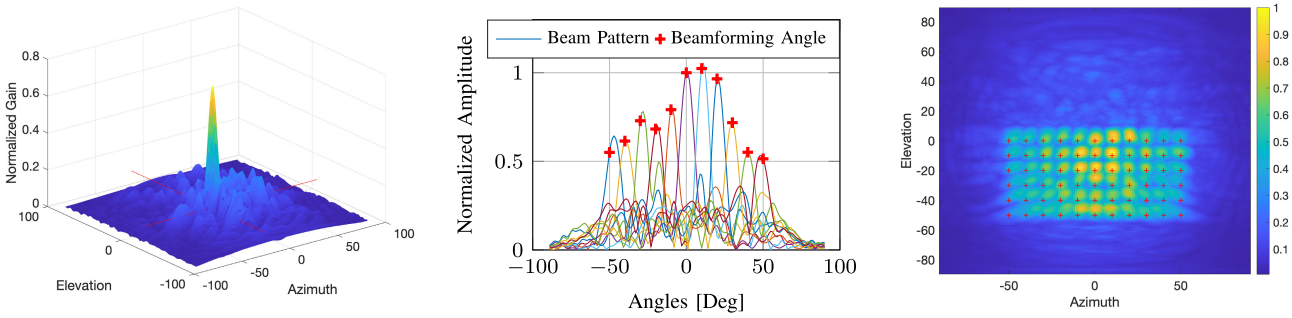

(a) (b) (c)

Fig. 3. Visualization of beam pattern measurements collected from the chamber: (a) 3D beam pattern for scanning angle at $[-20°, -20°]$; (b) Visualization of 2D beam patterns (11 codewords) when elevation angle is $0°$; (c) Visualization of 3D beam patterns (6×11 codewords, and the red cross indicates ideal beamforming angle).

TABLE III
BEAM PATTERN CALIBRATION RESULTS (IN TERMS OF BEAM SIMILARITY S_{R}, ANGLE ERROR E_{A}, AND CODEBOOK GAIN LOSS E_{C})

	Model	S_{R}[%]	E_{A}[°]	E_{C}[dB]
2D	M1 (uncalibrated)	80.60	1.0123	-1.4019
	M2	80.62	0.7926	-1.2367
	M3	80.40	2.5284	-1.5944
	M4 (L_{R}-AO)	96.45	0.1654	-1.1640
	M4 (L_{R}-GD)	**96.81**	0.1506	**-1.1636**
	M4 (L_{A})	95.81	**0.1086**	**-1.1636**
3D	M1 (uncalibrated)	63.72	5.1874	-2.7750
	M2	63.30	3.5235	-1.6316
	M3	78.79	2.3497	-3.2833
	M4 (L_{R}-AO)	95.65	0.9559	**-1.5236**
	M4 (L_{R}-GD)	**97.30**	0.8906	-1.5250
	M4 (L_{A})	93.93	**0.8556**	-1.5241

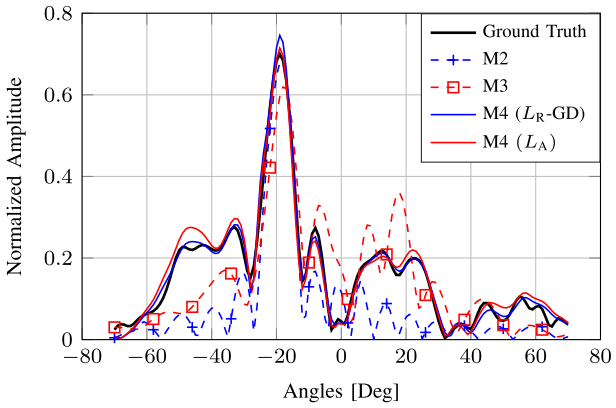

Fig. 4. Visualization of the reconstructed 2D beam patterns ($\bar{\varphi} = -20°$).

of the whole codebook in 3D calibration, we extract the largest gain (e.g., getting the maximum amplitude in the first dimension of the reshaped measurement dataset $\bar{\mathbf{B}}_{\mathrm{3D}}$) at certain angles as shown in Fig. 3 (c). We can clearly see the offset between the main lobe direction and the expected beamforming direction $\bar{\mathbf{\Phi}}$ (red cross markers), necessitating the need for calibration.

C. Calibration Performance Evaluation

The calibration methods described in this work are implemented in 2D and 3D scenarios. The comparison of different calibration methods on various performance metrics and models is shown in Table III. We notice that the calibration model M4, which considers estimating both the beamforming matrix $\mathbf{W}$ and channel gain matrix $\mathbf{\Gamma}$, achieves the best performance. Furthermore, the implementation of the loss function L_{A} further improves AEL, showing the effectiveness of the proposed loss function. We also noticed that the calibration error of 3D beam patterns is much larger than the 2D benchmark, and the improvement using AEL is limited. This is due to the higher dimension of calibration parameters that produces a large number of local minima, which affect the gradient-based calibration processes and lead to suboptimal solutions. In summary, the calibration method in this work can improve the angle estimation performance from $1.01°/5.19°$ to $0.11°/0.86°$ in 2D/3D scenarios, respectively.

The visualization of one specific calibrated 2D beam pattern (beamforming angle $\bar{\phi}^{\mathrm{az}} = -20°$) is shown in Fig. 4. Here, we omit M1 and M4 (L_R) due to the better performance of M2 and M4 (L_{R}-GD), respectively. Despite the superior performance of L_{R}-based calibrations over L_{A} in REL, the reconstructed beam pattern based on L_{A} is closer to the ground truth beam pattern in the main lobe, which is also reflected from other beam patterns that are not visualized. The visualization of calibrated 3D beam patterns (beamforming angle $\bar{\boldsymbol{\varphi}} = [-20°, -20°]^{\top}$) is shown in Fig. 5. The calibrated beam patterns in Fig. 5(c) and Fig. 5(d) can capture the features of ground truth much better than the uncalibrated one in Fig. 5(b). It is also seen that there are some outliers in AEL-based calibration on edge angles, which is due to the selection of anchor angles. The heatmap of angle estimation bias using the calibrated beam pattern is shown in Fig. 6, where the error level in all areas of interest can be largely reduced using the calibrated beam pattern.

D. Evaluation of Calibration Parameters

Due to the high calculation complexity using 3D beam data, we next focus on 2D beam pattern calibration and evaluate the impact of different parameters on calibration model M4.

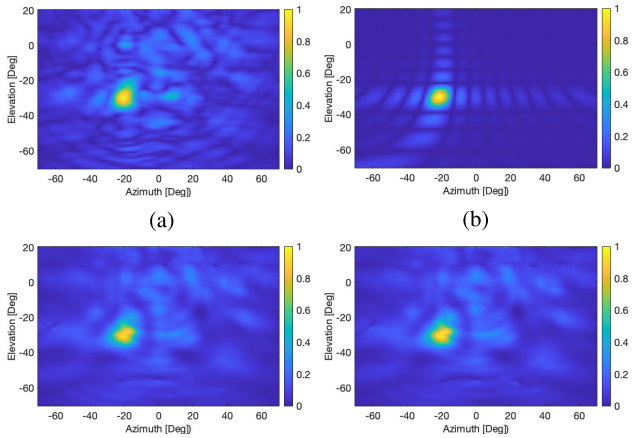

Fig. 5. Visualization of the reconstructed 3D beam patterns.

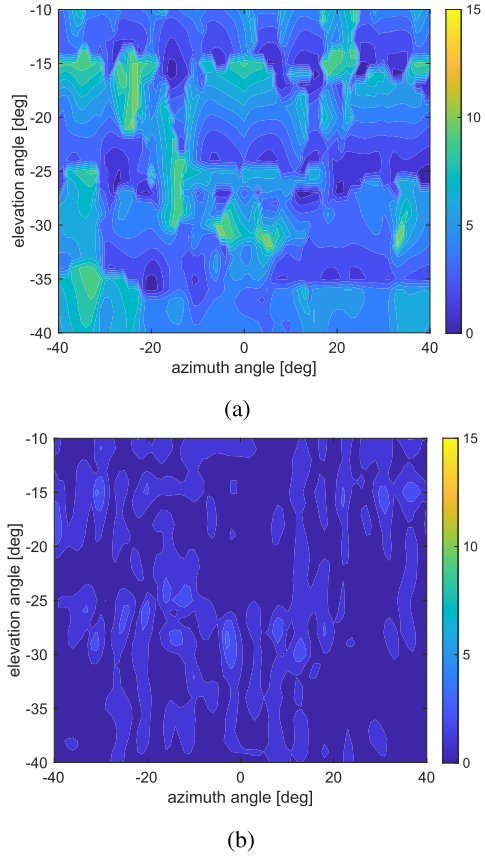

Fig. 6. Visualization of angle estimation errors before and after calibration.

We first assess the performance improvement using GD-based method compared with AO in REL-based calibration, as shown in Fig. 7. It is shown that the AO-based benchmark cannot converge well even with a sufficient number of iterations. In contrast, the GD-based method performs better with sufficient iterations and appropriate parameters. Specifically, a smaller mini-batch size requires a larger learning rate compared with processing all the measurement data at the same time. However, when the learning rate is too high, performance will be affected with oscillating loss, as shown in the curve with

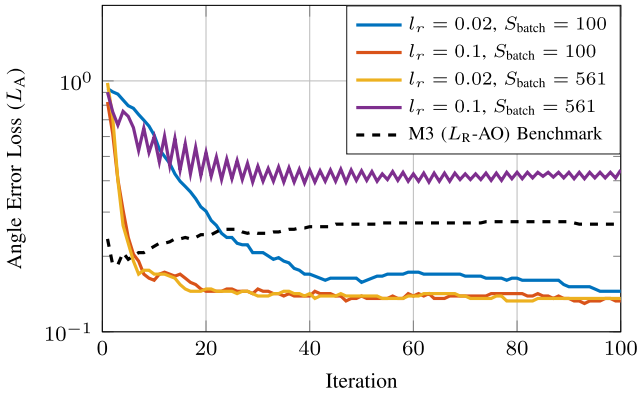

Fig. 7. Evaluation of different parameters using REL-based calibration (GD).

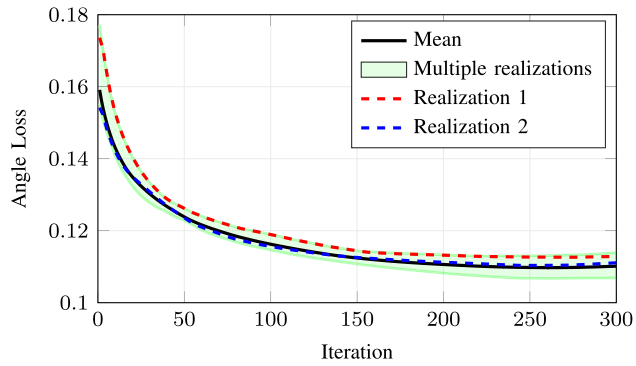

Fig. 8. AEL-based calibration with different initial codebooks $\mathbf{W}$ obtained using REL-based calibration.

$l_r = 0.1$ with the whole batch processing. It is foreseen that more advanced optimizers can be adopted for better performance, which is beyond the scope of this work.

With a calibrated beam based on L_{R}, AEL-based calibration can be performed. The evaluation of 20 different initial beamforming matrices $\mathbf{W}$ is shown in Fig. 8. Specifically, multiple realizations are visualized in the green area, with two specific realizations and mean loss plotted in dashed and solid curves. It is seen that the initial point directly affects calibration performance. Nevertheless, the proposed AEL-based calibration loss function can stably decrease the angle error in general.

For more practical consideration, we evaluate the impact of measurement noise on calibration. In this simulation, the BS is located at $[0, 0]$ m, and the UE moves from $[10, -30]$ m to $[10, 30]$ m along the line $x = 10$ m, with samples taken every 0.2 m along the y-axis. Three scatterers are evenly spaced along the y-range $[-30, 30]$ m at $x = 10$, and each scatterer is surrounded by 5 scattering points randomly distributed within a 1-meter radius circle centered at the scatterer. With different transmit power, the calibration performance (using angle loss) of M4-AEL is shown in Fig. 9 (a). Benchmarked against the scenario without noise and MPCs, the angle loss in noise-free calibration with MPCs increases the angle error from $0.21°$ to $0.33°$. The blue, yellow, and red curves combine the effects of received signal noise and the MPCs, showing that the calibration performance will be affected by strong MPCs (e.g., RCS = 10). As for the effect of signal noise,

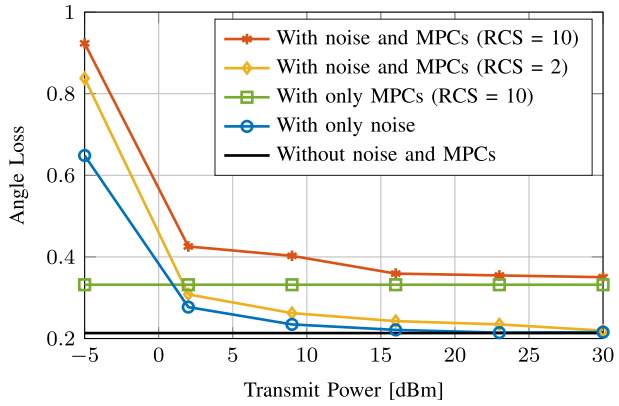

(a)

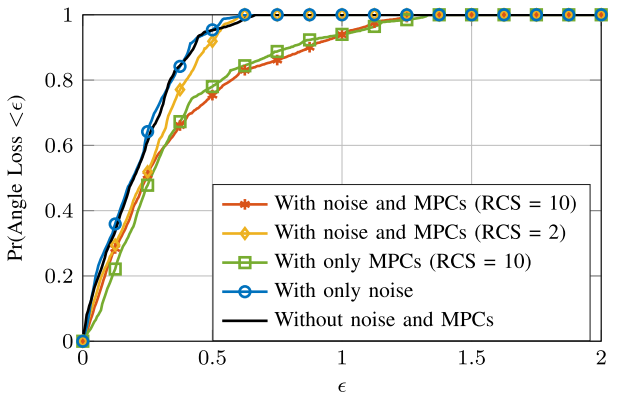

(b)

Fig. 9. Evaluation of the impacts of MPCs and transmit power on calibration performance. (a) Angle loss vs. transmit power; (b) CDF of the angle loss under different scenarios.

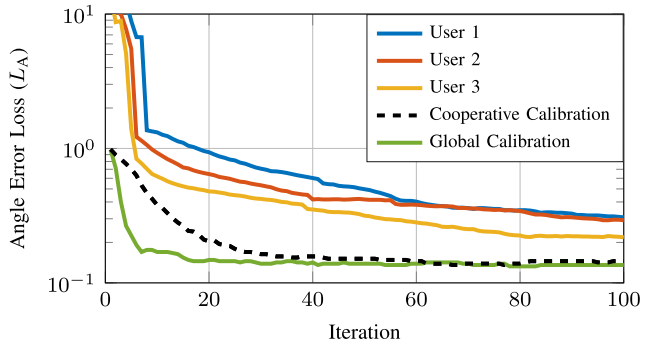

Fig. 10. Angle error loss evaluation for local calibration, cooperative calibration, and global calibration.

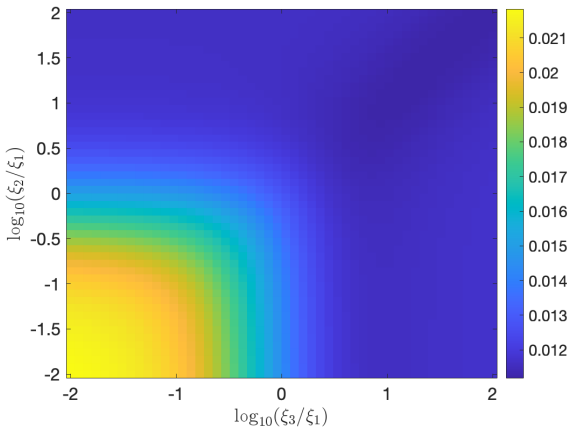

Fig. 11. Weights selection for global fusion.

it can be mitigated by increasing transmit power. We further investigate different calibration scenarios at the transmit power of 15 dBm. The CDF of angle estimation error is shown in Fig. 9 (b), highlighting a large gap caused by MPCs in the range of $0.2 \leq \epsilon \leq 1.2$. The performance degradation observed under strong scatterers reflects the impact of model mismatch between the single-path calibration formulation and the true multipath channel. Extending the framework to incorporate multipath-aware likelihood modeling is left for future work.

E. Cooperative Calibration

We further evaluate the performance using a cooperative calibration strategy, where $M = 3$ UEs process the local dataset to obtain a local beam pattern, which is then used for global fusion. The total dataset $T = 561$ is randomly split into 3 subsets with $T_1 = 100$, $T_2 = 200$, and $T_3 = 261$. The AELs for all the users using local calibrated results are shown in Fig. 10, benchmarked by the global calibration with all of the measurements (solid green curve). The cooperative calibration result is shown in the dashed black curve. For each point of the fused results, it reflects merging the calibrated local parameters after i iterations $\mathbf{W}_{m,i}$ with equal coefficients as described in (46). It is shown that with a sufficient number of iterations, cooperative calibration can achieve comparable performance as the global calibration strategy with a much reduced communication overhead when the measurements are large (reduced to $M \times G \times N$ from $M \times G \times T$ in terms of complex entries). Note that the calibration performance is also decided by the coverage of the data, and calibration strategies that consider the UE trajectory can be discussed in future work.

The evaluation of different weighting factors is shown in Fig. 11. Instead of using equal weights as $\xi_1 = \xi_2 = \xi_3 = 1/3$ in Fig. 10, we take ξ_1 as the reference and choose ξ_2 and ξ_3 from $\xi_1/100$ to $100\xi_1$ and visualize the AEL. As can be inferred from the figure, large values of ξ_2 and ξ_3 result in a better calibration performance (shown in green). This is also verified from Fig. 10 that UE 1 has the worst performance, and should be allocated a small weight. However, these results only demonstrate the effectiveness of the cooperative strategy. More optimized weighting factor values can be investigated, e.g., based on a Bayesian framework.

VI. Conclusion

This work presents a comprehensive framework for beam pattern calibration tailored to ISAC systems, prioritizing angular sensing accuracy over traditional pattern similarity metrics. A novel sensing-oriented metric based on angle estimation bias, derived through minimization of the KL divergence, is introduced to evaluate calibration quality. To

enable gradient-based optimization, a corresponding differentiable loss function is developed, supporting scalable and effective calibration across multiple user devices. Experimental validation using measured beam patterns from an anechoic chamber setup confirms the practical effectiveness of the proposed models and algorithms. Furthermore, the cooperative calibration strategy demonstrates that distributed updates from multiple UEs can achieve performance on par with centralized methods while significantly reducing communication overhead. These results establish a solid foundation for robust and adaptive beam calibration in future ISAC-enabled 6G systems. Looking ahead, future work should consider calibration algorithms that account for multipath propagation and non-ideal, frequency-dependent beam patterns in wideband systems. In addition, the proposed framework may also be applicable to mechanically reconfigurable architectures such as movable intelligent surfaces, where element displacement and alignment tolerances can exacerbate pattern mismatch. Extending the framework to such platforms is an interesting direction for future work.

APPENDIX A
GRADIENT DERIVATIONS FOR L_{A}

Recall the loss function L_{A} defined as

$$L_{\mathrm{A}} = \frac{\sum_{t,s} \rho_{t,s} \left|e_{t,s}\right|^2}{\sum_{t,s} \rho_{t,s}} = \frac{\sum_{t,s} \rho_{t,s} \left|u_{t,s} - \breve{u}_{t,s}\right|^2}{\sum_{t,s} \rho_{t,s}}, \tag{47}$$

where $u_{t,s} = \mathbf{b}_t^{\mathsf{H}} \mathbf{y}_s / \|\mathbf{b}_t\|$, $\breve{u}_{t,s} = \mathbf{y}_t^{\mathsf{H}} \mathbf{y}_s / \|\mathbf{y}_t\|$, $\mathbf{b}_t = \gamma_t \mathbf{W}^{\mathsf{H}} \mathbf{a}_t$, $\mathbf{a}_t = \mathbf{a}(\boldsymbol{\vartheta}_t)$. By using Wirtinger calculus, the gradient with respect to the conjugate of the matrix variable $\mathbf{W}^*$ can be calculated as

$$\frac{\partial L_{\mathrm{A}}}{\partial \mathbf{W}^*} = \frac{\sum_{t,s} \rho_{t,s} \left[(u_{t,s} - \breve{u}_{t,s})^* \frac{\partial u_{t,s}}{\partial \mathbf{W}^*} + (u_{t,s} - \breve{u}_{t,s}) \frac{\partial u_{t,s}^*}{\partial \mathbf{W}^*} \right]}{\sum_{t,s} \rho_{t,s}}. \tag{48}$$

We further define $u_{t,s} = p_{t,s}/q_t$ with $p_{t,s} = \gamma_t^* \mathbf{a}_t^{\mathsf{H}} \mathbf{W} \mathbf{y}_s$ and $q_t = |\gamma_t| \|\mathbf{W}^{\mathsf{H}} \mathbf{a}_t\|$. Using the quotient rule yields

$$\frac{\partial u_{t,s}}{\partial \mathbf{W}^*} = \frac{q_t \frac{\partial p_{t,s}}{\partial \mathbf{W}^*} - p_{t,s} \frac{\partial q_t}{\partial \mathbf{W}^*}}{q_t^2}, \tag{49}$$

$$\frac{\partial u_{t,s}^*}{\partial \mathbf{W}^*} = \frac{q_t \frac{\partial p_{t,s}^*}{\partial \mathbf{W}^*} - p_{t,s}^* \frac{\partial q_t}{\partial \mathbf{W}^*}}{q_t^2} \tag{50}$$

where

$$\frac{\partial p_{t,s}}{\partial \mathbf{W}^*} = 0, \quad \frac{\partial p_{t,s}^*}{\partial \mathbf{W}^*} = \gamma_t \mathbf{a}_t \mathbf{y}_s^{\mathsf{H}}, \quad \frac{\partial q_t}{\partial \mathbf{W}^*} = \frac{|\gamma_t|^2 \mathbf{a}_t \mathbf{a}_t^{\mathsf{H}} \mathbf{W}}{2 q_t}. \tag{51}$$

And the final expression is given by

$$\begin{aligned} \frac{\partial L_{\mathrm{A}}}{\partial \mathbf{W}^*} &= \frac{\sum_{t,s} \rho_{t,s} (u_{t,s} - \breve{u}_{t,s})^* \left(- \frac{u_{t,s} |\gamma_t|^2 \mathbf{a}_t \mathbf{a}_t^{\mathsf{H}} \mathbf{W}}{2 q_t^2} \right)}{\sum_{t,s} \rho_{t,s}} \\ &\quad + \frac{\sum_{t,s} \rho_{t,s} (u_{t,s} - \breve{u}_{t,s}) \left(\frac{\gamma_t \mathbf{a}_t \mathbf{y}_s^{\mathsf{H}}}{q_t} - \frac{u_{t,s}^* |\gamma_t|^2 \mathbf{a}_t \mathbf{a}_t^{\mathsf{H}} \mathbf{W}}{2 q_t^2} \right)}{\sum_{t,s} \rho_{t,s}} \\ &= \frac{\sum_{t,s} \rho_{t,s} \left[\frac{\gamma_t}{q_t} e_{t,s} \mathbf{a}_t \mathbf{y}_s^{\mathsf{H}} - \frac{|\gamma_t|^2}{q_t^2} \Re\{e_{t,s} u_{t,s}^*\} \mathbf{a}_t \mathbf{a}_t^{\mathsf{H}} \mathbf{W} \right]}{\sum_{t,s} \rho_{t,s}}. \end{aligned} \tag{52}$$

For the scalar variable γ_t^*, we compute the derivative as

$$\frac{\partial L_{\mathrm{A}}}{\partial \gamma_t^*} = \frac{\sum_{s=1}^{S} \rho_{t,s} \left(e_{t,s}^* \frac{\partial u_{t,s}}{\partial \gamma_t^*} + e_{t,s} \frac{\partial u_{t,s}^*}{\partial \gamma_t^*} \right)}{\sum_{t,s} \rho_{t,s}}. \tag{53}$$

Based on $\frac{\partial p_{t,s}}{\partial \gamma_t^*} = \frac{p_{t,s}}{\gamma_t^*}$, $\frac{\partial p_{t,s}^*}{\gamma_t^*} = 0$ and $\frac{\partial q_t}{\gamma_t^*} = \frac{q_t}{2\gamma_t^*}$, we can have

$$\frac{\partial u_{t,s}}{\partial \gamma_t^*} = \frac{q_t \frac{\partial p_{t,s}}{\partial \gamma_t^*} - p_{t,s} \frac{\partial q_t}{\partial \gamma_t^*}}{q_t^2} = \frac{p_{t,s}}{2\gamma_t^* q_t} = \frac{1}{2} \frac{u_{t,s}}{\gamma_t^*}, \tag{54}$$

$$\frac{\partial u_{t,s}^*}{\partial \gamma_t^*} = - \frac{p_{t,s}^*}{2\gamma_t^* q_t} = - \frac{1}{2} \frac{u_{t,s}^*}{\gamma_t^*}. \tag{55}$$

Hence, the gradient with respect to γ_t^* is given as

$$\frac{\partial L_{\mathrm{A}}}{\partial \gamma_t^*} = \frac{\sum_s \rho_{t,s} \left(e_{t,s}^* u_{t,s} - e_{t,s} u_{t,s}^* \right)}{2\gamma_t^* \sum_{t,s} \rho_{t,s}} \tag{56}$$

$$= \frac{j \sum_s \rho_{t,s} \Im\{e_{t,s}^* u_{t,s}\}}{\gamma_t^* \sum_{t,s} \rho_{t,s}}. \tag{57}$$

REFERENCES

[1] F. Liu et al., "Integrated sensing and communications: Toward dual-functional wireless networks for 6G and beyond," *IEEE J. Sel. Areas Commun.*, vol. 40, no. 6, pp. 1728–1767, Jun. 2022.

[2] H. Chen, H. Sarieddeen, T. Ballal, H. Wymeersch, M. Alouini, and T. Y. Al-Naffouri, "A tutorial on terahertz-band localization for 6G communication systems," *IEEE Commun. Surveys Tuts.*, vol. 24, no. 3, pp. 1780–1815, 3rd Quart., 2022.

[3] 3GPP, "NR; stage 2 functional specification of user equipment (UE) positioning in NG-RAN," *3GPP TS 38.305: NR, V16.6.0, Release 16*, 2025. https://portal.3gpp.org

[4] R. Mendrzik, H. Wymeersch, G. Bauch, and Z. Abu-Shaban, "Harnessing NLOS components for position and orientation estimation in 5G millimeter wave MIMO," *IEEE Trans. Wireless Commun.*, vol. 18, no. 1, pp. 93–107, Jan. 2019.

[5] P. Zheng, T. Ballal, H. Chen, H. Wymeersch, and T. Y. Al-Naffouri, "Coverage analysis of joint localization and communication in THz systems with 3D arrays," *IEEE Trans. Wireless Commun.*, vol. 23, no. 5, pp. 5232–5247, May 2024.

[6] M. Lotti, G. Pasolini, A. Guerra, F. Guidi, R. D'Errico, and D. Dardari, "Radio SLAM for 6G systems at THz frequencies: Design and experimental validation," *IEEE J. Sel. Topics Signal Process.*, vol. 17, no. 4, pp. 834–849, Jul. 2023.

[7] K. Stylianopoulos et al., "Distributed intelligent sensing and communications for 6G: Architecture and use cases," in *Proc. Joint Eur. Conf. Netw. Commun. 6G Summit (EuCNC/6G Summit)*, Jun. 2025, pp. 583–588.

[8] P. Zheng, H. Chen, T. Ballal, M. Valkama, H. Wymeersch, and T. Y. Al-Naffouri, "JrCUP: Joint RIS calibration and user positioning for 6G wireless systems," *IEEE Trans. Wireless Commun.*, vol. 23, no. 6, pp. 6683–6698, Jun. 2024.

[9] H. Chen et al., "Modeling and analysis of OFDM-based 5G/6G localization under hardware impairments," *IEEE Trans. Wireless Commun.*, vol. 23, no. 7, pp. 7319–7333, Aug. 2023.

[10] F. Wen, N. Garcia, J. Kulmer, K. Witrisal, and H. Wymeersch, "Tensor decomposition based beamspace ESPRIT for millimeter wave MIMO channel estimation," in *Proc. IEEE Global Commun. Conf. (GLOBECOM)*, Dec. 2018, pp. 1–7.

[11] A. Pourafzal, H. Huang, V. Pettersson, M. F. Keskin, and H. Wymeersch, "FLEX: Low-complexity 5D beamspace channel estimation for mmWave MIMO-OFDM," in *Proc. 33rd Eur. Signal Process. Conf. (EUSIPCO)*, Sep. 2025, pp. 920–924.

[12] R. S. P. Sankar, S. P. Chepuri, and Y. C. Eldar, "Beamforming in integrated sensing and communication systems with reconfigurable intelligent surfaces," *IEEE Trans. Wireless Commun.*, vol. 23, no. 5, pp. 4017–4031, May 2024.

[13] R. Ghazalian et al., "Calibration in RIS-aided integrated sensing, localization and communication systems," *IEEE Wireless Commun.*, vol. 33, no. 2, pp. 200–207, Apr. 2026.

[14] M. Pan et al., "In situ calibration of antenna arrays for positioning with 5G networks," *IEEE Trans. Microw. Theory Techn.*, vol. 71, no. 10, pp. 4600–4613, Oct. 2023.

[15] R. Pohlmann, S. Zhang, E. Staudinger, A. Dammann, and P. A. Hoeher, "Simultaneous localization and calibration for cooperative radio navigation," *IEEE Trans. Wireless Commun.*, vol. 21, no. 8, pp. 6195–6210, Aug. 2022.

[16] T. Takahashi, H. Miyashita, Y. Konishi, and S. Makino, "Theoretical study on measurement accuracy of rotating element electric field vector (REV) method," *Electron. Commun. Jpn.*, vol. 89, no. 1, pp. 22–33, Jan. 2006.

[17] T. Takahashi, Y. Konishi, S. Makino, H. Ohmine, and H. Nakaguro, "Fast measurement technique for phased array calibration," *IEEE Trans. Antennas Propag.*, vol. 56, no. 7, pp. 1888–1899, Jul. 2008.

[18] T. Takahashi, Y. Konishi, and I. Chiba, "A novel amplitude-only measurement method to determine element fields in phased arrays," *IEEE Trans. Antennas Propag.*, vol. 60, no. 7, pp. 3222–3230, Jul. 2012.

[19] R. Long, J. Ouyang, F. Yang, W. Han, and L. Zhou, "Fast amplitude-only measurement method for phased array calibration," *IEEE Trans. Antennas Propag.*, vol. 65, no. 4, pp. 1815–1822, Apr. 2017.

[20] R. Long, J. Ouyang, F. Yang, W. Han, and L. Zhou, "Multi-element phased array calibration method by solving linear equations," *IEEE Trans. Antennas Propag.*, vol. 65, no. 6, pp. 2931–2939, Jun. 2017.

[21] F. Zhang, W. Fan, Z. Wang, Y. Zhang, and G. F. Pedersen, "Improved over-the-air phased array calibration based on measured complex array signals," *IEEE Antennas Wireless Propag. Lett.*, vol. 18, pp. 1174–1178, 2019.

[22] Z. Wang, F. Zhang, H. Gao, O. Franek, G. F. Pedersen, and W. Fan, "Over-the-air array calibration of mmWave phased array in beam-steering mode based on measured complex signals," *IEEE Trans. Antennas Propag.*, vol. 69, no. 11, pp. 7876–7888, Nov. 2021.

[23] G. Gradoni and M. Di Renzo, "End-to-end mutual coupling aware communication model for reconfigurable intelligent surfaces: An electromagnetic-compliant approach based on mutual impedances," *IEEE Wireless Commun. Lett.*, vol. 10, no. 5, pp. 938–942, May 2021.

[24] W. Zhang and Y. Jiang, "Over-the-air phase calibration of reconfigurable intelligent surfaces," *IEEE Wireless Commun. Lett.*, vol. 12, no. 4, pp. 664–668, Apr. 2023.

[25] A. Fadakar, M. F. Keskin, H. Chen, and H. Wymeersch, "Mutual coupling-aware localization for RIS-assisted ISAC systems," *IEEE Trans. Cognit. Commun. Netw.*, vol. 11, no. 5, pp. 2938–2954, Oct. 2025.

[26] Z. Zhou, Z. Wei, J. Ren, Y. Yin, G. F. Pedersen, and M. Shen, "Transfer-learning-assisted multielement calibration for active phased antenna arrays," *IEEE Trans. Antennas Propag.*, vol. 71, no. 2, pp. 1982–1987, Feb. 2023.

[27] J. Miguel Mateos-Ramos, C. Häger, M. Furkan Keskin, L. Le Magoarou, and H. Wymeersch, "Model-based end-to-end learning for multi-target integrated sensing and communication under hardware impairments," *IEEE Trans. Wireless Commun.*, vol. 24, no. 3, pp. 2574–2589, Mar. 2025.

[28] Q. Wu et al., "Integrating movable antennas and intelligent reflecting surfaces (MA-IRS): Fundamentals, practical solutions, and ISAC," *IEEE Wireless Commun.*, vol. 33, no. 1, pp. 155–163, Feb. 2026.

[29] D. Xu, X. Yu, D. W. K. Ng, A. Schmeink, and R. Schober, "Robust and secure resource allocation for ISAC systems: A novel optimization framework for variable-length snapshots," *IEEE Trans. Commun.*, vol. 70, no. 12, pp. 8196–8214, Dec. 2022.

[30] Y. Xu, D. Xu, and S. Song, "Sensing-assisted robust SWIPT for mobile energy harvesting receivers in networked ISAC systems," *IEEE Trans. Wireless Commun.*, pp. 2094–2109, Dec. 2024.

[31] C. A. Balanis, *Antenna Theory: Analysis and Design*. Hoboken, NJ, USA: Wiley, 2016.

[32] M. Li et al., "RIS beam calibration for ISAC systems: Modeling and performance analysis," 2025, *arXiv:2505.15403*.

[33] H. Chen, P. Zheng, M. F. Keskin, T. Al-Naffouri, and H. Wymeersch, "Multi-RIS-enabled 3D sidelink positioning," *IEEE Trans. Wireless Commun.*, vol. 23, no. 8, pp. 8700–8716, Aug. 2024.

[34] F. Zhang, Z. Wang, T.-H. Loh, Y. Gui, S. Tang, and W. Fan, "Multiprobe-enabled over-the-air calibration of millimeter-wave antenna arrays: Concepts and experimental validations," *IEEE Antennas Propag. Mag.*, vol. 66, no. 4, pp. 14–25, Aug. 2024.

[35] Z. Zheng, Q. Wu, W. Chen, and G. Hu, "Two-timescale design for movable antenna-enabled multiuser MIMO systems," *IEEE Trans. Commun.*, vol. 73, no. 11, pp. 10554–10571, Nov. 2025.

[36] *3GPP TR 38.827 V16.8.0: Study on Radiated Metrics and Test Methodology for the Verification of Multi-antenna Reception Performance of NR User Equipment (UE) (Release 16) (accessed on 15-Oct-2025)*, document TR 38.827, 3GPP, Sep. 2022.

[37] C. Ozturk, M. F. Keskin, H. Wymeersch, and S. Gezici, "RIS-aided near-field localization under phase-dependent amplitude variations," *IEEE Trans. Wireless Commun.*, vol. 22, no. 8, pp. 5550–5566, Aug. 2023.

[38] Y. Zhang, P. Khanduri, I. Tsaknakis, Y. Yao, M. Hong, and S. Liu, "An introduction to bilevel optimization: Foundations and applications in signal processing and machine learning," *IEEE Signal Process. Mag.*, vol. 41, no. 1, pp. 38–59, Apr. 2024.

[39] D. H. Brandwood, "A complex gradient operator and its application in adaptive array theory," *IEE Proc. H Microw., Opt. Antennas*, vol. 130, no. 1, pp. 11–16, 1983.

[40] J. Nocedal and S. J. Wright, *Numerical Optimization*. Cham, Switzerland: Springer, 2006.

[41] D. P. Bertsekas, *Nonlinear Programming*. Belmont, MA, USA: Athena Scientific, 1995.

[42] Y. Dorrazehi, A. Khaleel, A. Sezgin, A. V. Guglielmi, and S. Tomasin, "A novel RIS-based base station architecture for sensing-assisted communications," *Authorea Preprints*, 2026.

[43] J. Hyeon Park, S. Hyun Kim, M. Miftahul Amri, N. Minh Tran, D. In Kim, and K. W. Choi, "Uplink MIMO communications with RIS-integrated base station: Modeling and experiments," *IEEE Internet Things J.*, vol. 12, no. 10, pp. 14150–14171, May 2025.

[44] P. Li et al., "Design of low-cost single-layer 2-bit reflective programmable metasurface based on folded ground," *IEEE Trans. Microw. Theory Techn.*, vol. 71, no. 8, pp. 3455–3465, Aug. 2023.